SYNTHESIS, CRYSTALLIZATION, X-RAY STRUCTURAL CHARACTERIZATION AND SOLID STATE ASSEMBLY OF A CYCLIC HEXAPEPTOID WITH PROPARGYL AND METHOXYETHYL SIDE CHAINS

Authors

Consiglia Tedesco[a]*, Eleonora Macedi[a], Alessandra Meli[a], Giovanni Pierri[a], Giorgio Della Sala[a], Christina Drathen[b], Andrew N. Fitch[b], Gavin B. M. Vaughan[b], Irene Izzo[a] and Francesco De Riccardis[a]

[a]Dept. of Chemistry and Biology "A. Zambelli", University of Salerno, via Giovanni Paolo II 132, Fisciano, 84084, Italy

[b] European Synchrotron Radiation Facility, CS40220, Grenoble Cedex 9, 38043, France

Correspondence email: ctedesco@unisa.it

Synopsis The synthesis and the structural characterization of a cyclic hexapeptoid with four methoxyethyl and two propargyl side chains allowed to discuss the solid state assembly of a hydrate crystal form (form **I**) and an anhydrous crystal form (form **II**). The relative amounts of form **I** and form **II** in the as-purified product were determined by Rietveld refinement and depend on the purification procedures.

Abstract The synthesis and the structural characterization of a cyclic hexapeptoid with four methoxyethyl and two propargyl side chains allowed to disclose the presence of a hydrate crystal form (form **I**) and an anhydrous crystal form (form **II**). The relative amounts of form **I** and form **II** in the as-purified product were determined by Rietveld refinement and depend on the purification procedures. In crystal form **I** peptoid molecules assemble in a columnar arrangement by means of side chain to backbone C≡CH···OC hydrogen bonds. In the anhydrous crystal form **II** cyclopeptoid molecules form ribbons by means of backbone to backbone CH_2···OC hydrogen bonds, thus mimicking beta-sheet secondary structures in proteins. In both crystal forms side chains act as joints among the columns or the ribbons and contribute to the stability of the whole solid state assembly. Water molecules in the hydrate crystal form **I** bridge columns of cyclic peptoid molecules, providing a more efficient packing.

Keywords: Cyclic peptoids; Solid state assembly; Single crystal X-ray diffraction; Rietveld refinement

1. Introduction

Macrocycles constitute an expanding class of natural and synthetic members with unlimited potentials (Gokel *et al.*, 1992; Dietrich *et al.*, 1993; Böhmer, 1995; Ambrosi *et al.*, 2009a; Ambrosi *et al.*, 2009b, Ambrosi *et al.*, 2010).

Cyclic peptoids represent a recent and promising addition to the realm of macrocycle compounds for their biostability, potential diversity and elegant architectures (Culf & Ouellette, 2010; Izzo *et al.*, 2011; Sun & Zuckermann, 2013; Gangloff *et al.*, 2016).

In general, peptoids differ from peptides for the side chain position, which is shifted along the peptide backbone to give *N*-substituted oligoglycines (Figure 1).

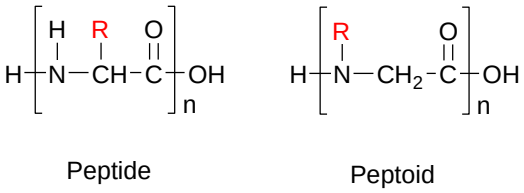

Figure 1 Comparison between peptide and peptoid structures.

Cyclic peptoids show several properties: they are resistant to proteolytic degradation (Yoo *et al.*, 2010), they promote the transport across a phospholipid membrane (De Cola *et al*., 2009) and show promising antimicrobial activity (Comegna *et al.*, 2010; Huang *et al.*, 2012; Huang *et al.*, 2013). Moreover, they are used also as phase transfer catalysts with performances comparable to crown ethers (Della Sala *et al.*, 2013; Schettini *et al.* 2014; Schettini *et al.*, 2016) and as scaffold for hybrid glyco-peptoid systems (M. L. Lepage *et al.*, 2014; M. L. Lepage *et al.*, 2016).

The lack of the amide protons prevents the formation of NH···OC hydrogen-bonds and *cis*/*trans* conformations of tertiary amide bonds are almost isoenergetic (Figure 2).

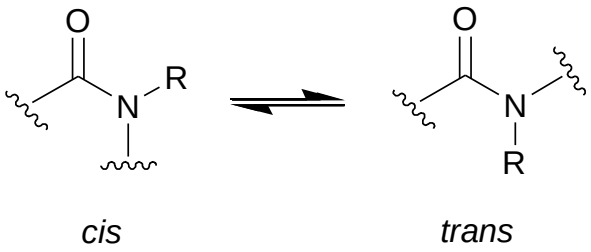

Figure 2 *Cis*/*trans* conformational isomerism in tertiary amides.

In particular in a recent survey we highlighted that in the solid state cyclic hexapeptoids exhibit a *cctcct* sequence of *cis* (*c*) and *trans* (*t*) conformations of amide groups with the only notable exception of metal coordinated compounds (Tedesco *et al.*, 2014). We also concluded that methoxyethyl and propargyl side chains are the most effective in inducing a columnar arrangement of peptoid macrocycles. In fact, they act as pillars and extend vertically with respect to the macrocycle plane interacting with the backbone atoms of the macrocycles below and above (Maulucci *et al.*, 2008; Izzo *et al.*, 2013; Meli *et al.*, 2016; Tedesco *et al.*, 2016).

In our effort to elucidate the role of propargyl and methoxyethyl side chains in the solid state assembly of cyclic peptoids, we aimed at the synthesis of a cyclohexamer with two propargyl and four methoxyethyl side chains: cyclo-(Npa-Nme_2)$_2$, compound **1** reported in Figure 3 (Npa=*N*-(propargyl)glycine, Nme= *N*-(methoxyethyl)glycine).

Noteworthy, the analogous peptoid cyclohexamer substituted with four propargyl and two methoxyethyl side chains features a peculiar solid state dynamic behaviour (Meli *et al.*, 2016). In detail, upon guest removal it undergoes a reversible single crystal-to-single crystal transformation involving a drastic *conformational* change with a movement of 113° of two propargyl side chains. This generates new stabilizing CH-pi interactions and forms an unprecedented reversible "CH-pi zipper".

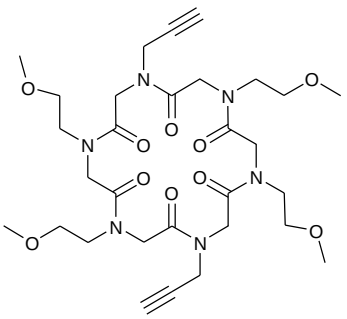

1

Figure 3 Cyclo-(Npa-Nme_2)$_2$ **1**, Npa=*N*-(propargyl)glycine, Nme= *N*-(methoxyethyl)glycine.

Here we report the synthesis, the crystallization and the structural characterization by X-ray powder and single crystal diffraction of two crystal forms of compound **1**.

Moreover, we exploited Hirshfeld surface analysis (McKinnon *et al.*, 2004; Spackman & Jayatilaka, 2009) together with lattice energy calculations (Gavezzotti, 2002; Gavezzotti, 2003; Gavezzotti 2011) to describe the packing motifs in the two crystal forms.

2. Experimental

2.1. Synthesis and purification

The synthesis and purification procedures for the preparation of the cyclic peptoid compound **1** are reported in the following sections. Two batches, indicated as BATCH1 and BATCH2, were obtained in two subsequent times by following the described procedure (Figure 4). See also the Supporting Information for general procedures and further details.

2.1.1. Sub-monomer solid-phase synthesis of the linear peptoid

The 2-chlorotrityl chloride resin (α-dichlorobenzhydryl-polystyrene cross-linked with 1% DVB (divinylbenzene); 100 – 200 mesh; 1.5 mmol g^{-1}, 0.30 g, 0.45 mmol) was swelled in dry CH_2Cl_2 (3 mL) for 45 min and washed twice with dry DMF (3.0 mL). The first submonomer was linked to the resin by adding bromoacetic acid (100 mg, 0.72 mmol) in dry CH_2Cl_2 (3.0 mL) and DIPEA (392 μL, 2.20 mmol) on a shaker platform for 60 min at room temperature, followed by washing with dry CH_2Cl_2 (3 × 1 min) and then with DMF (3 × 1 min). A solution of the commercially available propargyl amine (288 μl, 4.50 mmol) in dry DMF (3 mL) was added to the bromoacetylated resin. The mixture was left on a shaker platform for 30 min at room temperature, then the resin was washed with DMF (3 × 1 min), CH_2Cl_2 (3 × 1 min) and then again with DMF (3 × 1 min). Subsequent bromoacetylation reactions were accomplished by reacting the aminated oligomer with a solution of bromoacetic acid (624 mg, 4.50 mmol) and DIC (766 μL, 4.95 mmol) in dry DMF (3.0 mL) for 40 min at room temperature. The filtrated resin was washed with DMF (3 × 1 min), CH_2Cl_2 (3 × 1 min), DMF (3 × 1 min) and treated again with the amine under the same conditions reported above. A solution of the commercially available methoxyethyl amine (391 μl, 4.50 mmol) in dry DMF (3 mL) was added to the bromoacetylated resin. This cycle of reactions was iterated until the desired chain length was accomplished and the target oligomer obtained. The cleavage was performed by treating twice the resin, previously washed with CH_2Cl_2 (3 × 1 min), with a solution of HFIP in CH_2Cl_2 (20% v/v, 6.0 mL) on a shaker platform at room temperature for 30 min and 5 min, respectively. The resin was then filtered away and the combined filtrates were concentrated *in vacuo*. The final product was dissolved in 50% acetonitrile in HPLC grade water and analyzed by RP-HPLC [purity >95%; conditions: 5 → 100% A in 30 min for the all oligomers (A, 0.1% TFA in acetonitrile, B, 0.1% TFA in water); flow: 1.0 mL min^{-1}, 220 nm]. The linear oligomer was subjected to the cyclization reaction without further purification.

Linear precursor: 210 mg, 70% (crude residue); t_R : 9.0 min (chromatogram: Figure S1a in the Supporting Information)
ESI-MS (positive, *m/z*): 669.05 $[M + H]^+$.

2.1.2. Cyclization reactions: synthesis of compound 1

A solution of the linear peptoid (0.30 mmol), previously co-evaporated three times with toluene, was prepared under nitrogen in dry DMF (20.0 mL). The mixture was added dropwise to a stirred solution of HATU (465 mg, 1.22 mmol) and DIPEA (330 μL, 1.90 mmol) in dry DMF (82.0 mL) by a syringe pump in 12 h, at room temperature in anhydrous atmosphere. After 24 h the resulting mixture was concentrated *in vacuo*, diluted with CH_2Cl_2 (100 mL), washed with a solution of HCl (1.0 M, 50.0 mL). The mixture was extracted with CH_2Cl_2 (2 × 100.0 mL) and the combined organic phases were washed with water (150.0 mL), dried over anhydrous $MgSO_4$, filtered and concentrated *in vacuo*. The cyclic product was dissolved in 50% acetonitrile in HPLC grade water and analyzed by RP-HPLC [purity >95% conditions: 5% → 100% A in 30 min (A, 0.1% TFA in acetonitrile, B, 0.1% TFA in water); flow: 1 mL min^{-1}, 220 nm; t_R 10.4 min min (chromatogram: Figure S1b in the Supporting Information).

The crude was dissolved in hot acetonitrile and crystallized by slowly cooling the acetonitrile solution (90 mg, 31%, BATCH1). The synthesis was repeated in the same conditions and a second batch of compound **1** was obtained (90 mg, 31%, BATCH2).

ESI-MS (positive, *m*/*z*): 651.2 ($[M + H]^+$).

^{1}H NMR: (400 MHz, $CDCl_3$, mixture of rotamers) δ: 5.28-3.88 (12H, m, COC*H*$_2$N); 3.59-3.24 (32H, m, NC*H*$_2$CH$_2$OCH$_3$, NCH$_2$C*H*$_2$OCH$_3$, NCH$_2$CH$_2$OC*H*$_3$, NC*H*$_2$CCH); 2.38-2.17 (2H, m, NCH$_2$CC*H*); see Figure S2 in the Supporting Information.

^{13}C NMR: (100 MHz, $CDCl_3$, mixture of rotamers, broad signals) δ: 170.6, 169.8, 169.6, 169.5, 169.4, 169.2, 169.1, 168.7, 78.8, 78.7, 78.6, 78.5, 78.4, 73.8, 73.6, 73.0, 72.8, 72.3, 72.0, 71.8, 71.6, 71.5, 71.0, 70.5, 70.4, 70.2, 70.0, 69.7, 69.5, .68.8, 68.6, 59.3, 59.1, 59.0, 58.7, 58.5, 58.4, 58.3, 52.0, 50.6, 50.3, 50.2, 50.0, 79.9, 49.8, 49.6, 49.5, 49.2, 49.0, 48.9, 48.8, 48.6, 48.5, 48.2, 48.0, 47.9, 47.8, 47.7, 47.6, 47.6, 47.5, 47.4, 47.3, 47.3, 47.2, 47.1, 47.0, 46.8, 46.6, 46.4, 46.2, 46.0, 45.8, 45.7, 45.6, 43.5, 43.2, 42.6, 37.5, 37.4, 37.3, 37.2, 36.9, 36.8, 36.6, 36.2, 36.0, 35.8, 35.7, 35.5, 35.4, 35.3, 31.8, 29.6. See Figure S3 in the Supporting Information.

2.2. Crystallization

Form I. Two crystallization trials provided single crystals suitable for X-ray diffraction.

In the first trial compound **1** (5 mg from BATCH1) was dissolved in 1.5 mL of chloroform and 0.75 mL of isopropanol were added. White needle-like crystals obtained by complete evaporation after 1 week were suitable only for synchrotron X- ray diffraction studies.

The same results were obtained by using compound **1** from BATCH2 (5 mg) with the same solvents. In this last case it was necessary to warm up the crystallization vial to obtain a complete dissolution.

Form II. Compound **1** (5 mg of BATCH1) was kneaded with 5.0 μL ethylene glycol (EG) in a mortar and then dissolved in 1.5 mL of chloroform and 0.75 mL of isopropanol (ratio 2:1). White platy crystals were obtained by slow evaporation after 2 weeks.

2.3. Single crystal X-ray diffraction

A crystal of form **I** as obtained from chloroform/isopropanol (0.35 mm x 0.025 mm x 0.010 mm) was mounted on a MiTeGen microloop™ and measured at 100 K at the European Synchrotron Radiation Facility beam line ID11. Data reduction was performed with the Bruker programs SMART, Saint, SADABS (Bruker, 2012). Lorentz and polarization correction were applied to the data.

A crystal of form **II** (0.45 mm x 0.34 mm x 0.23 mm) suitable for laboratory X-ray diffraction were selected and mounted on a MiTeGen microloop™ with Paratone® N. In both cases data collection was performed at 100 K with a Rigaku AFC7S diffractometer equipped with a Mercury^2 CCD detector using graphite monochromated Mo$K\alpha$ radiation. Data were corrected for Lorentz, polarization and absorption. Data reduction was performed with the crystallographic package CrystalClear (Rigaku-Molecular Structure Corp., 2006).

The structures were solved by direct methods using the program SIR2014 (Burla *et al.*, 2015) and refined by means of full matrix least-squares based on F^2 using the program SHELXL (Sheldrick, 2015).

X-seed (Barbour, 2001) was used as GUI. Crystal structures were drawn using Mercury (Macrae *et al.*, 2008). ORTEP drawings were made by OLEX (Dolomanov *et al.*, 2009).

For all compounds non-hydrogen atoms were refined anisotropically. Hydrogen atoms were positioned geometrically and included in structure factors calculations but not refined, with the only exception of water hydrogen atoms in form **I**.

Water hydrogen atoms were located from difference Fourier maps and their coordinates refined.

Refinement details are summarized in Table 1. Relevant geometric details are reported in Tables 2, 3, and 4.

2.4. X-ray powder diffraction

Synchrotron radiation X-ray powder diffraction experiments were performed at the high-resolution powder diffraction beam line ID22 at the ESRF, Grenoble, France (Fitch *et al.*, 2004). X-ray powder diffraction patterns were collected selecting X-rays from an insertion device source with a double-crystal Si(111) monochromator. Selected wavelengths were 0.849893(4) Å and 0.427488(5) Å for BATCH1 and BATCH2, respectively.

Small amounts of powder samples were introduced into thin walled 0.7 mm diameter borosilicate glass capillaries.

Each capillary containing either BATCH1 or BATCH2 sample was mounted on the diffractometer and spinned during measurements in order to improve randomisation of the orientations of the individual crystallites.

Data were collected at 100 K using an Oxford Cryosystems Cryostream cold nitrogen gas blower.

Raw data were normalized against monitor counts and detector efficiencies and rebinned into steps of 0.005º 2θ. Numerous short 1minute scans were collected to investigate the occurrence of any radiation damage and - in case - avoid it by translating the capillary by ~2.1 mm in the beam.

2.5. Thermal analyses

DSC measurements were performed on a TA DSC-Q20 instrument under a purified N_2 flow (50 mL/min) by heating heated at a rate of 1 ºC/min.

Single crystals (1.00 mg) of form **I** obtained by slow evaporation of a chloroform/isopropanol solution of BATCH1 were sealed in aluminium pans and heated at a rate of 1 ºC/min.

TGA measurements were performed on a TA Q500 TGA instrument using single crystals of form **I** (1.035 mg) under a purified N_2 flow (50 mL/min) by heating at 1.0 ºC/min.

Single crystals (1.40 mg) of form **II** obtained by slow evaporation of a EG/chloroform/isopropanol solution of BATCH1 were sealed in aluminium pans.

2.6. Packing analysis

2.6.1. Hirshfeld surface analysis

Hirshfeld surface analysis and related fingerprint plots have been performed with Crystal Explorer 3.1 (Wolff *et al.*, 2013).
The lengths of X–H bonds are normalized using standard X–H distances from Allen *et al.* (1995). Thus, reported X–H distances and X···H contacts are not equal to those calculated from the original cif files.

2.6.2. CLP-Pixel calculations

The lattice energy of all the crystal forms was calculated using the CLP-Pixel package (Gavezzotti, 2002; Gavezzotti, 2003; Gavezzotti 2011). The total lattice energy is partitioned into its coulombic, polarization, dispersion and repulsion contributions (Table 5). In CLP-Pixel, the coulombic terms are handled by Coulomb's law, while the polarization terms are calculated in the linear dipole approximation, with the incoming electric field acting on local polarizabilities and generating a dipole with its associated dipole separation energy; dispersion terms are simulated in London's inverse sixth power approximation, involving ionization potentials and polarizabilities; repulsion is presented as a modulated function of wavefunction overlap. Selected motifs in the crystal packing of both crystal forms were analyzed by means of their interaction energies (Table 5).

In both crystal forms the centres of gravity of the cyclopeptoid molecules are located on crystallographic inversion centres. Therefore, to consider a whole cyclopeptoid molecule in the CLP calculations, the space group symmetry was lowered to *P*1 for crystal form **I** and $P2_1$ for crystal form **II**. As for the crystal form **I** in *P*1 the asymmetric unit contains four molecules (two cyclopeptoid molecules and two water molecules). Since the PIXEL module is limited to structures with no more than two independent molecules, four molecular pairs were considered and processed separately four times. This procedure, previously applied by Solanko & Bond (2011) and Shukla *et al.* (2014), allows to consider all relevant pairwise intermolecular interactions.
The lengths of X–H bonds are normalized using standard X–H distances from Allen *et al.* (1995). Thus, the values given throughout the discussion refer to the re-calculated structures.

2.7. Rietveld Refinement

Rietveld refinement was accomplished using the program TOPAS Academic (Coelho, 2007).
Data in the Q-range 0.20- 4.00 $Å^{-1}$ were included, comprising 461 Bragg reflections for crystal form **I** and 888 for crystal form **II**, which were modelled using a pseudo-Voigt function. No absorption correction was applied to the data.
Refinement was performed considering as variables the cell parameters, zero-shift parameter, profile and background parameters (12 terms Chebyshev polynomial function). Preferred orientation for the phase corresponding to the crystal form **I** was taken into account by means of spherical harmonics. The atomic and displacement parameters were taken from the corresponding structure models obtained from the single-crystal X-ray diffraction data and were not refined.
Final indices are reported in Table 6.

3. Results and discussion

3.1. Synthesis and purification

The synthesis of the cyclic hexamer, cyclo-$(Npa\text{-}Nme_2)_2$ **1**, Npa=*N*-(propargyl)glycine, Nme= *N*-(methoxyethyl)glycine, was performed starting from the linear precursor, prepared on solid-phase, using 2-chlorotrityl chloride resin as support, following the well known sub-monomeric approach, introduced by Zuckermann *et. al.* (1992).

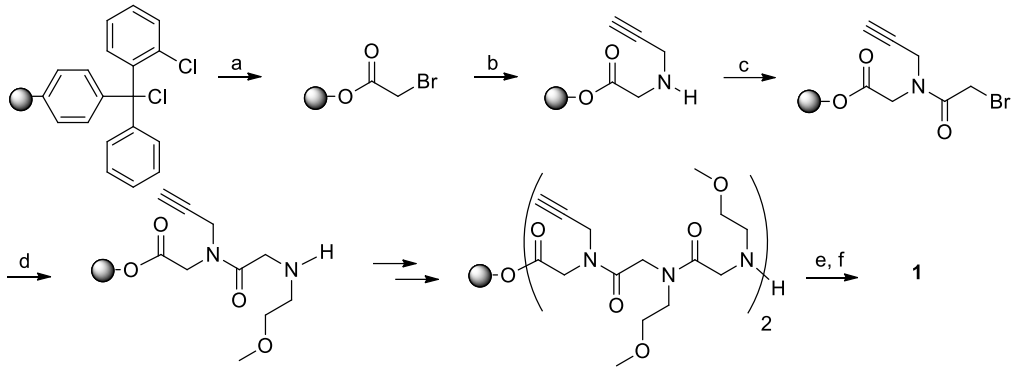

Figure 4 (a) bromoacetic acid, DIPEA, CH_2Cl_2; (b) propargyl amine, DMF; (c) bromoacetic acid, DIC, DMF; (d) methoxyethyl amine, DMF (e) CH_2Cl_2/HFIP (4/1); (f) HATU, DIPEA, DMF. ; DIPEA = *N*,*N*-diisopropylethylamine; HATU = 1-[bis(dimethylamino)methylene]-1*H*-1,2,3-triazolo[4,5-*b*]pyridinium hexafluorophosphate 3-oxide; DIC = *N*,*N*′-diisopropyl carbodiimide; HFIP = 1,1,1,3,3,3-hexafluoro-2-propanol.

Cleavage from resin, followed by cyclization in high dilution condition afforded compound **1** in 31 % overall yield (Figure 4).

Purification of the cyclic derivative is a delicate step in the preparation of cyclopeptoids. Different methods may be used and have to be tailored on the specific product. In our case dissolution in hot acetonitrile and crystallization by slowly cooling of the acetonitrile solution afforded a white crystalline powder. In order to obtain a bigger amount of material two subsequent syntheses were performed leading to two batches, named BATCH1 and BATCH2. Preliminary ^{1}H-NMR spectra of the two batches resulted to be identical (Figure S2 in the Supporting Information).

3.2. X-Ray Powder Diffraction

High-resolution X-ray powder diffraction (XRPD) measurements were performed at ID22 ESRF beam line at 100 K on BATCH1 and BATCH2 samples. XRPD profiles are reported in Figure 5 and result to be significantly different indicating the presence of multiple phases. Phase identification in the two samples was possible thanks to the availability of single crystals of the corresponding crystalline forms. This also allowed to perform a quantitative phase analysis (*vide ultra*).

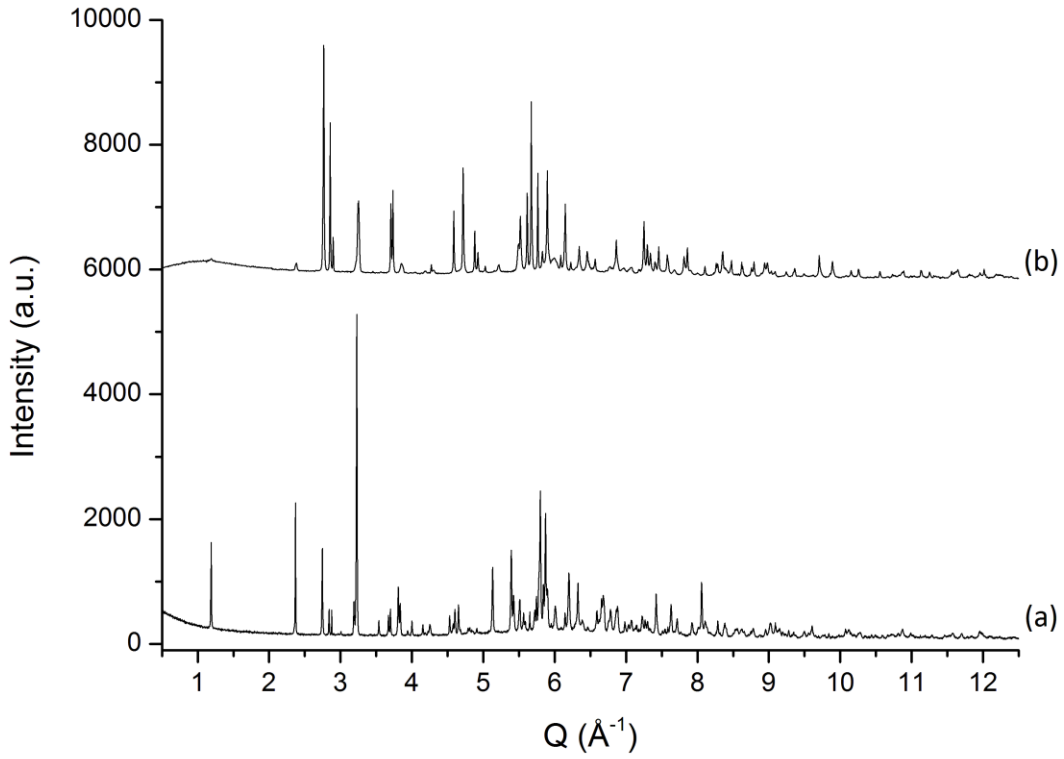

Figure 5 XRPD profiles of BATCH1 (a) and BATCH2 (b).

3.3. Single Crystal X-ray Diffraction

In order to obtain single crystals of **1** suitable for X-ray diffraction analysis we performed several crystallization trials, using both BATCH1 and BATCH2.

By complete evaporation of a solution of **1** in chloroform/isopropanol (2:1 ratio) we obtained rather small (<50 μm) crystals suitable for synchrotron X-ray diffraction, which correspond to a hydrate crystal form (indicated as form **I**).

By kneading compound **1** with a drop of ethylene glycol (EG) and adding chloroform/isopropanol (2:1 ratio) we obtained by slow evaporation crystals of an anhydrous form (named form **II**).

Notably the use of EG as dehydrating agent allowed us to obtain a new crystal form despite the crystallization solvents and their ratio were the same.

Relevant crystallographic data and structure refinement details for both crystal forms **I** and **II** are listed in Table 1.

Figures 6 and 7 show the X-ray molecular structures of the cyclopeptoid molecules respectively for crystal forms **I** and **II**.

Table 1 Crystal data and structure refinement details for **1** as crystal forms **I** and **II**.

Crystal form	**I**	**II**
Solvents	$CHCl_3$/i-PrOH	$CHCl_3$/i-PrOH/EG
Formula	$C_{30}H_{46}N_6O_{10} \cdot H_2O$	$C_{30}H_{46}N_6O_{10}$
Formula weight	668.74	650.73
System	triclinic	monoclinic
Space group	$P\bar{1}$	$P2_1/n$
a (Å)	8.363(4)	9.0367(17)
b (Å)	9.394(4)	10.6221(18)
c (Å)	21.648(10)	18.022(3)
α(°)	78.362(5)	90.00
β(°)	88.664(7)	102.661(4)
γ(°)	83.547(5)	90.00
V (Å^3)	1655.1(13)	1687.9(5)
Z	2	2
D_X (gcm^{-3})	1.342	1.280
μ (mm^{-1})	0.031	0.097
F_{000}	716	696
wavelength (Å)	0.29520	0.71073
R ($I>2\sigma_I$)	0.0730 (7288)	0.0606 (2516)
$_wR_2$ (all)	0.1954 (8341)	0.1733 (4342)
N. of param.	430	209
GooF	1.136	0.916
$\Delta\rho$ min/max (eÅ^{-3})	-0.38/0.71	-0.31/0.36

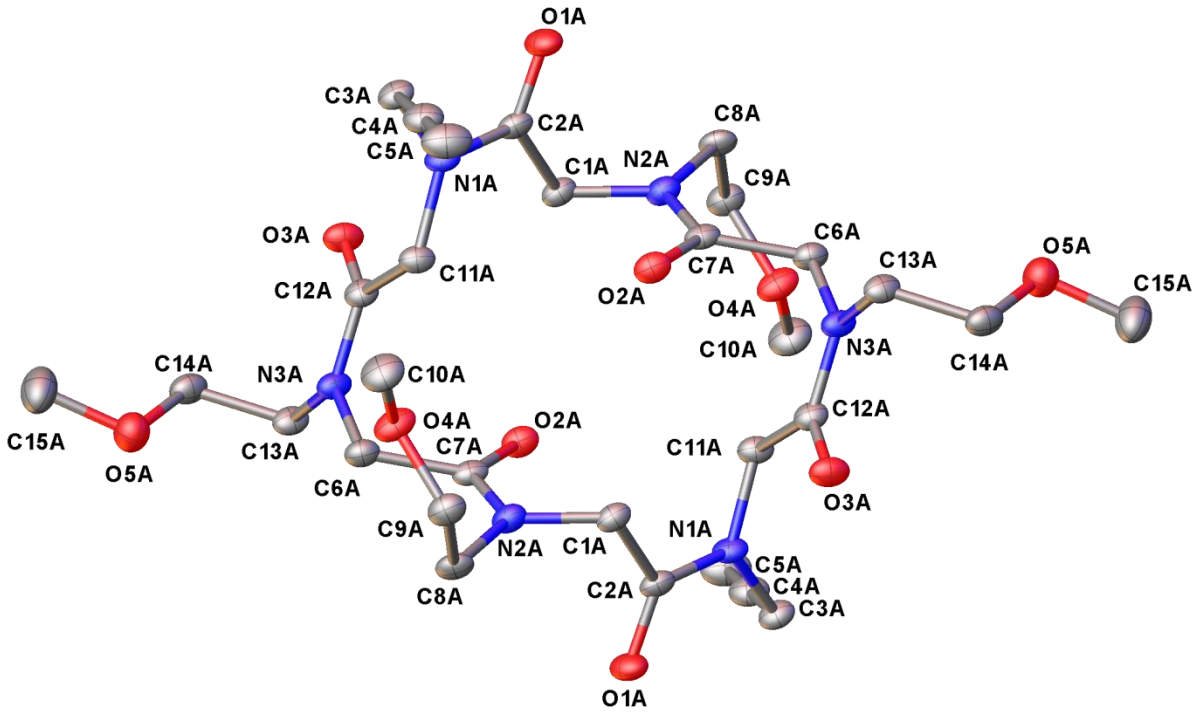

(a)

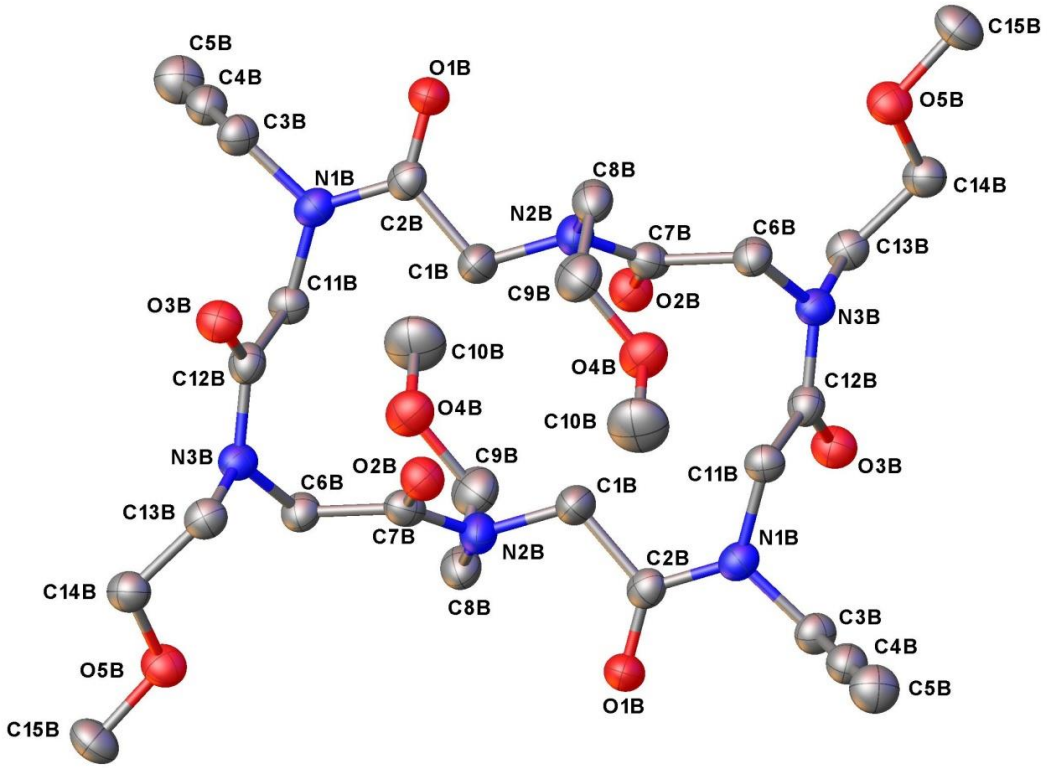

(b)

Figure 6 ORTEP with labelling scheme for crystal form **I** type A (a) and type B (b) cyclopeptoid molecules. Oxygen atoms in red, carbon in grey, nitrogen in blue. Hydrogen atoms are omitted for clarity.

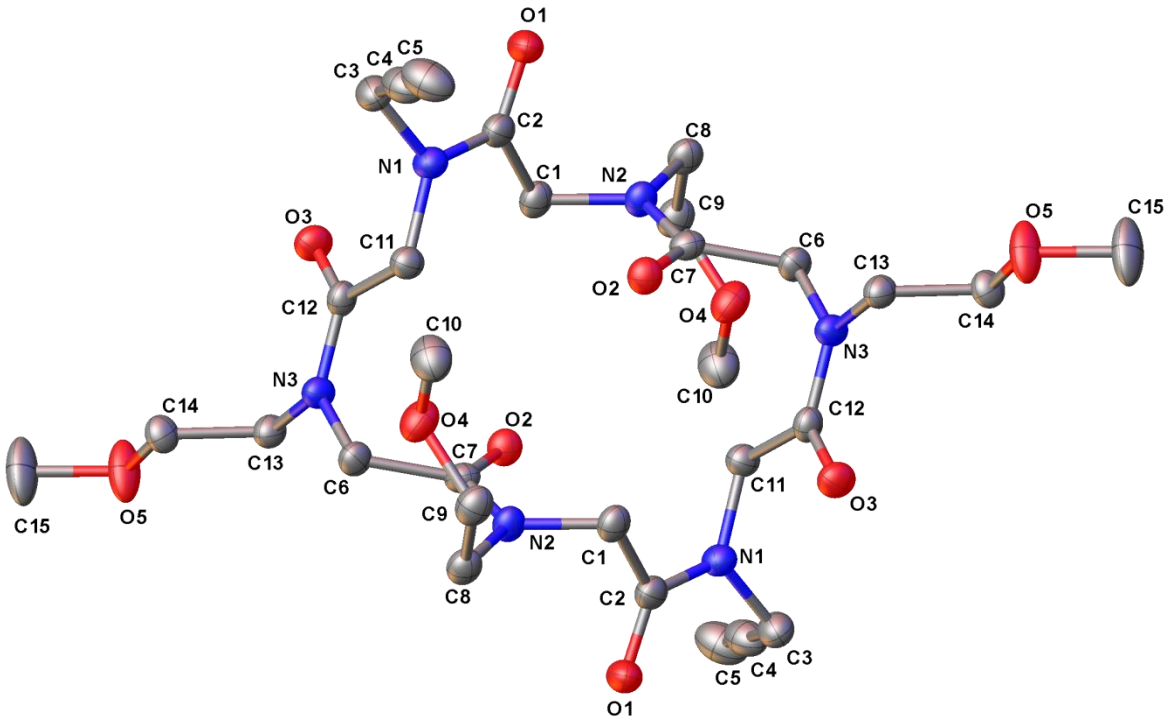

Figure 7 ORTEP with labelling scheme for the cyclopeptoid molecule in crystal form **II**. Oxygen atoms in red, carbon in grey, nitrogen in blue. Hydrogen atoms are omitted for clarity.

As for the hydrate crystal form **I** the unit cell contains two crystallographically independent cyclopeptoid molecules (indicated as type A and type B, respectively in blue and green in Figures 8 and S4 in the Supporting Information) and two water molecules. As for the anhydrous crystal form **II** the unit cell contains two cyclopeptoid molecules (Figures 9 and S5 in the Supporting Information).

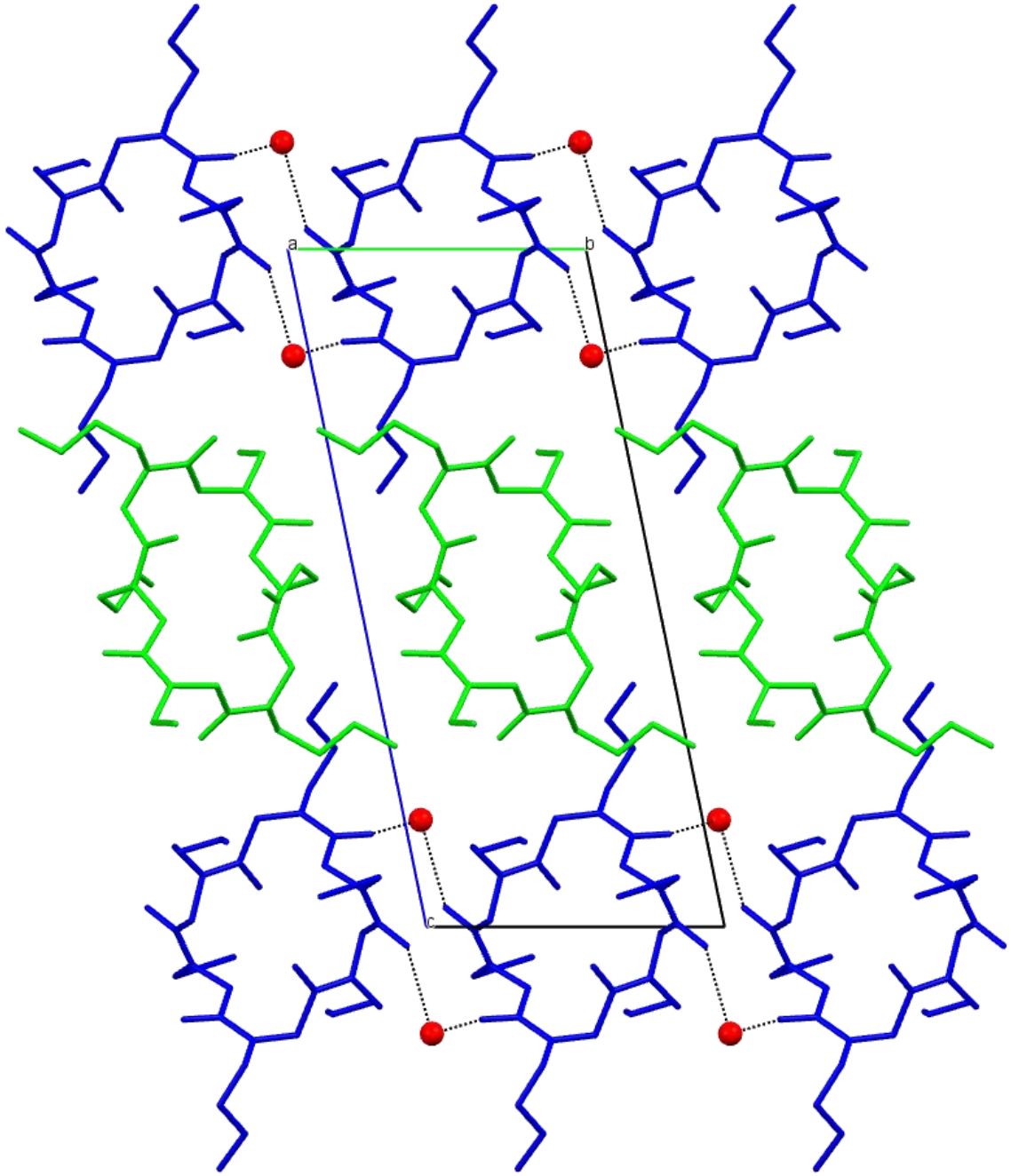

Figure 8 Crystal packing of form **I** as viewed along the *a* axis (see also Figure S4 in the Supporting Information). Type A molecules are shown in blue and type B molecules in green, water molecules in red. Hydrogen bonds are depicted as black dotted lines. Hydrogen atoms are omitted for clarity.

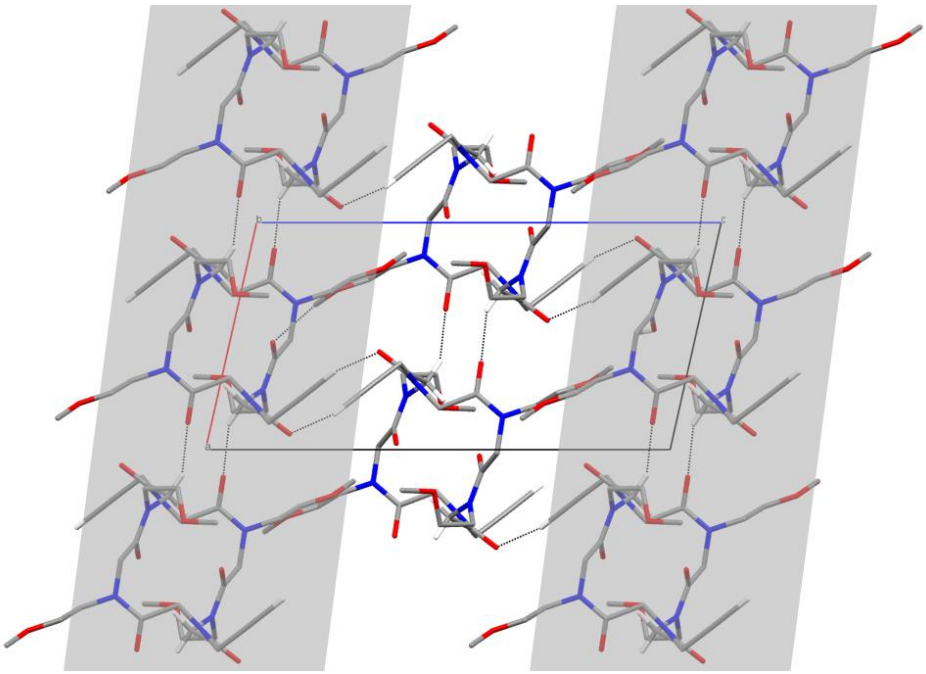

Figure 9 Crystal packing of form **II** as viewed along the *b* axis (see also Figure S5 in the Supporting Information). Intermolecular interactions are depicted as black dotted lines. Hydrogen atoms (except those involved in CH···O hydrogen bonds) are omitted for clarity. Oxygen atoms in red, carbon in grey, nitrogen in blue. Shaded and white areas highlight molecular ribbons shifted by 1/2 *b* as a consequence of the crystallographic screw axis.

In both crystal forms the peptoid macrocycle possesses a crystallographic inversion centre and exhibits a distorted *cctcct* conformation of the peptoid backbone, which assumes a rectangular shape defined by the four nitrogen atoms at the corners (N1A/N1B and N3A/N3B in crystal form **I** and N1 and N3 in crystal form **II**) as shown in Figures 10 and S6 in the Supporting Information.

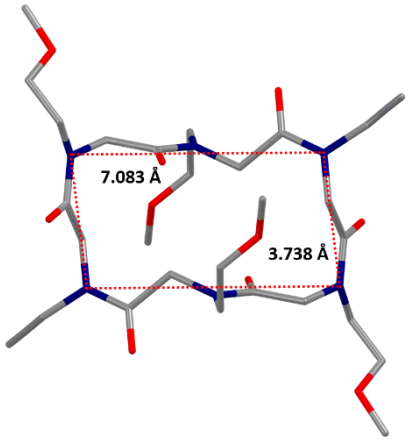

Figure 10 Rectangular shape of the macrocycle as in crystal form **I** type B molecule (see Figure S6 in the Supporting Information for type A molecule and crystal form **II** cyclopeptoid molecule). Hydrogen atoms have been omitted for clarity. Oxygen atoms in red, carbon in grey, nitrogen in blue.

In Table 2 we report the values of the rectangular widths and lengths of the macrocycles in crystal forms **I** and **II**. Notably the values of the lengths have a much higher variance than the widths. As for the crystal form **I**, the main difference between the two independent molecules, type A and type B, is due to the backbone. Type B molecules have a wider length with respect to type A molecules. Backbone atoms overlay gives a rmsd value of 0.647 Å (Figure S7 in the Supporting Information).

Table 2 Rectangular widths (Å) and lengths (Å) of the macrocycles in crystal forms **I** and **II**.

	Form I type A	**Form I** type B	**Form II**
Width (Å)	3.725	3.738	3.699
Length (Å)	6.032	7.083	6.082

As for the crystal form **II** the peptoid backbone is very similar to type A molecule in crystal form **I** (rmsd 0.0435 Å, Figure S8 in the Supporting Information).
The propensity to mimic reverse turn secondary structures in proteins (Yoo *et al.*, 2010; Shin *et al.*, 2007) was tested by the superposition of the peptoid backbone atoms respectively in form **I** (type A and B molecules) and form **II** with the corresponding peptide backbone atoms of idealized β-turns, types I and III (Venkatachalam, 1968; Crawford *et al.*, 1973). In Table 3 the corresponding rmsd values are reported for comparison.

Table 3 Superposition of peptoid backbone atoms with idealized β-turns peptide backbone atoms.

	Form **I** Molecule A rmsd (Å)	Form **I** Molecule B rmsd (Å)	Form **II** rmsd (Å)
Idealized type I β-turn	0.486	0.183	0.463
Idealized type III β-turn	0.360	0.395	0.345

Peptoid backbone atoms in form **I** (type A and B molecules) and form **II** (N2A/B, C7A/B, C6A/B, N3A/B, C12A/B, C11A/B, N1A/B, C2A/B, C1A/B, N2A/B and N2, C7, C6, N3, C12, C11, N1, C2, C1, N2) are superimposed with idealized type I and type III β-turn peptide backbone atoms (Cαi, Ci, Ni + 1, Cαi + 1, Ci + 1, Ni + 2, Cαi + 2, Ci + 2, Ni+3, and Cαi+3).

In all cases the peptoid backbone seems to adapt better to a type III β-turn structure, except for type B molecule of form **I**, which shows a very good agreement with a type I β-turn structure (Figures S9, S10 and S11 in the Supporting Information). In both crystal forms **I** and **II** two *trans* methoxyethyl and two *cis* propargyl side chains point vertically with respect to the macrocycle plane, while the

remaining *cis* propargyl side chains extend horizontally (Figures 11, 12 and S12 in the Supporting Information).

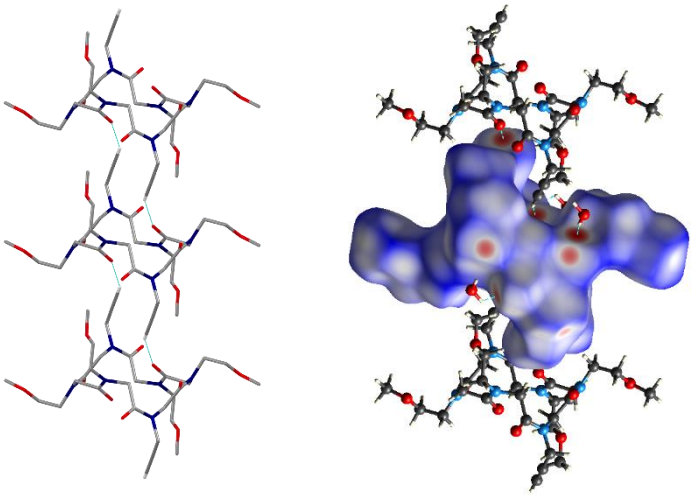

(a) (b)

Figure 11 Columnar interactions among type A molecules in crystal form **I** (motif 1 A-A) as viewed along the *b* axis. The corresponding Hirshfeld surface and hydrogen bonded water molecules are shown in (b). CO···HC and CO···HO hydrogen bonds are depicted as light blue dotted lines. Oxygen atoms in red, carbon in grey, nitrogen in blue. For the sake of clarity, in (a) only hydrogen atoms involved in the columnar interactions are reported.

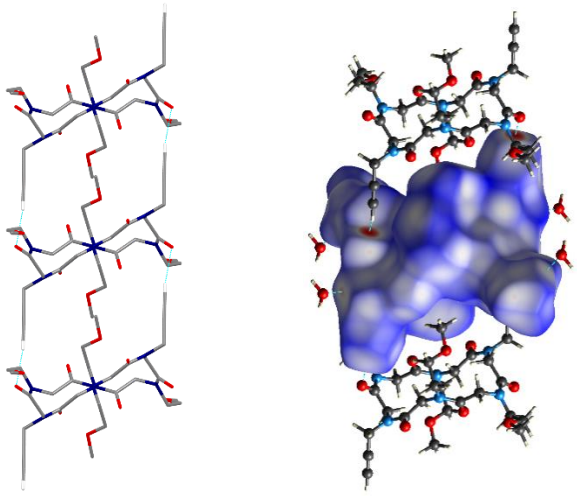

(a) (b)

Figure 12 Columnar interactions among type B molecules in crystal form **I** (motif 4 B-B) as viewed along the *b* axis. The corresponding Hirshfeld surface and hydrogen bonded water molecules are shown in (b). CO···HC and CO···HO hydrogen bonds are depicted as light blue dotted lines.

Oxygen atoms in red, carbon in grey, nitrogen in blue. For the sake of clarity, in (a) only hydrogen atoms involved in the columnar interactions are reported.

Table 4 Torsion angles (°) for crystal form **I** (type A and B molecules) and crystal form **II**.[a,b]

Residue[b]	ω			φ		
	I A	**I** B	**II**	**I** A	**I** B	**II**
Npa	-13.6(3)	-6.7(3)	-14.5(3)	77.3(2)	96.1(2)	80.0(2)
Nme1	167.36(15)	164.67(17)	167.95(16)	73.4(2)	122.9(2)	76.1(2)
Nme2	4.9(3)	25.5(3)	1.7(2)	67.6(2)	66.2(2)	70.2(2)
Residue[b]	**ψ**			**χ1**		
	I A	**I** B	**II**	**I** A	**I** B	**II**
Npa	-179.97(16)	-166.63(17)	-176.48(14)	106.4(2)	108.9(2)	103.5(2)
Nme1	133.17(17)	-179.98(18)	133.33(18)	101.6(2)	99.8(2)	101.0(2)
Nme2	-167.05(16)	-167.25(17)	-168.51(16)	76.4(2)	134.2(2)	96.14(19)

[a] As a consequence of the crystallographic and molecular inversion centre opposite side chains display values for the torsion angles which are identical but with opposite signs.

[b] Nme = *N*-(methoxyethyl)glycine, Npa = *N*-(propargyl)glycine, the *trans* methoxyethyl side chain is indicated as Nme1, the *cis* methoxyethyl side chain is indicated as Nme2 (Nme1 C8→C10; Nme2 C13→C15).

The values of the torsion angles in the macrocycles, according to Butterfoss *et al.* (2009), are reported in Table 4. Type A molecule in crystal form **I** and the cyclopeptoid molecule in crystal form **II** have very similar values. Main differences are in the values of φ and ψ torsion angles for the *trans* methoxyethyl residues (Nme1) and in the ω and χ_1 torsion angles for the *cis* methoxyethyl residues (Nme2).

3.4. Crystal packing analysis

The crystal packing in both crystal forms was analyzed by means of Hirshfeld surface analysis and intermolecular energy calculations in order to define the main interactions in the crystal.
As for crystal form **I** two Hirshfeld surfaces must be considered for type A and B molecules, respectively. Figures 11b and 12b map the normalized contact distance d_{norm} upon the Hirshfeld surfaces (McKinnon *et al.*, 2007) and highlight the significant difference in the number of contacts experienced by the two molecules. In particular, it is evident that type B molecules are involved in fewer close contacts than type A molecules (there are fewer red spots on the surface of type B

molecules). Moreover, for type B molecules the closest contacts are established only with molecules of the same type.

Intermolecular energy calculations for both crystal forms were performed by means of CLP-Pixel (Gavezzotti, 2002; Gavezzotti, 2003; Gavezzotti 2011) and are reported in Table 5.

Selected motifs in the crystal packing of both crystal forms were analyzed by means of their interaction energies calculated with the Pixel method (Table 5).

As for crystal form **I** the strongest interactions are related to motifs 1 A-A and 4 B-B (Table 5), which correspond to columns of type A molecules and type B molecules, respectively. Indeed both type A and B molecules align in a columnar arrangement along the shortest *a* axis, as shown in Figures 8, 11 and 12. This agrees with the analysis of the Hirshfeld surfaces for crystal form **I** (Figures 11b and 12b).

Intracolumnar interactions in type A molecules (motif 1 A-A in Table 5) consist of CO···HC hydrogen bonds involving the carbonyl oxygen atoms O2A and the terminal hydrogen atoms of the *cis* propargyl side chains (C5A), CO···HC = 2.09 Å; O···H-C = 150° (Figure 11). Intracolumnar interactions in type B molecules (motif 4 B-B in Table 5) consist of CO···HC hydrogen bonds involving the carbonyl oxygen atoms O3B and the terminal hydrogen atoms of the *cis* propargyl side chains (C5B), CO···HC = 2.16 Å; O···H-C = 170° (Figure 12).

Interactions between columns of type A molecules (motif 2 A-A) occur along the *b* axis by means of CO···HC interactions between the *cis* carbonyl oxygen atoms (O3A) and the methylene hydrogen atoms of the *trans* methoxyethyl side chains (C8A), CO···HC = 2.27 Å; O···H-C = 151° (Figure 13).

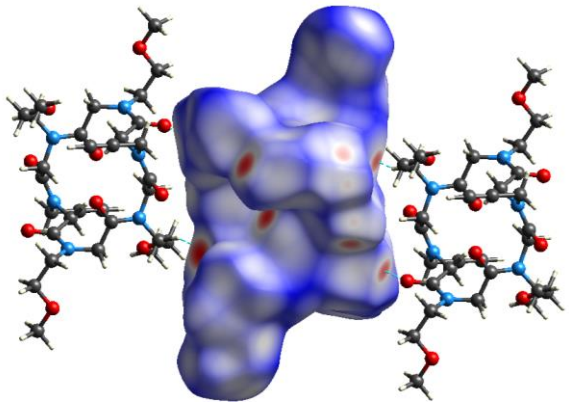

Figure 13 Intercolumnar interactions for type A molecules (motif 2 A-A). CO···HC hydrogen bonds are depicted as light blue dotted lines. Oxygen atoms in red, carbon atoms in grey, nitrogen atoms in blue and hydrogen atoms in white.

Interactions among columns of type B molecules (motif 5 B-B) occur along the *b* axis, by means of CO···HC interactions between the *cis* carbonyl oxygen atoms (O1B) and the methylene hydrogen atoms of the *trans* methoxyethyl side chains (C8B), (CO···HC = 2.57 Å; O···H-C = 162°) (Figure 14). Notably in this case the energetic contribution of columns of type B molecules (-70.6 kJ mol^{-1}) is greater than the energetic contribution of columns of type A molecules (-54.6 kJ mol^{-1}) in spite of the longer CO···HC distances for type B molecules (2.57 Å vs. 2.27 Å).

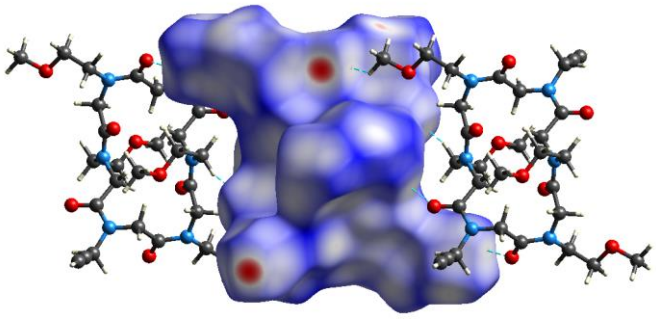

Figure 14 Intercolumnar interactions for type B molecules (motif 5 B-B). CO···HC hydrogen bonds are depicted as light blue dotted lines. Oxygen atoms in red, carbon atoms in grey, nitrogen atoms in blue and hydrogen atoms in white.

Moreover intracolumnar interactions of type B molecules are energetically equivalent to intercolumnar interactions of type B molecules (-77.5 and -70.6 kJ mol^{-1}), thus type B molecules are arranged in a two-dimensional fashion.

Interactions among type A and type B molecules (motif 6A-B) are less energetically important than interactions among molecules of the same type.

As for the water molecules they interact mainly with type A molecules by bridging *cis* carbonyl oxygen atoms O1A and O3A of two different type A molecules (motifs 10 A-W and 11 A-W and Figures 8, 11b, and 12b). Interactions among water molecules and type B molecules (motifs 12 B-W and 13 B-W) are less significant.

As for crystal form **II** the strongest interactions are related to motifs 1 and 2 (Table 5), whose energetic contribution is almost the same (-56.9 and -51.6 kJ mol^{-1}).

Motif 1 is made of molecules aligned side by side along the shortest axis (*a* axis) by means of backbone to backbone CH_2···OC hydrogen bond between the *cis* carbonyl oxygen atom O3 and a backbone methylene hydrogen atom (H1B) (CO···HC = 2.34 Å; O···H-C = 152°) (Figure 15). This molecular assembly represents the peptoid counterpart of beta-sheet secondary structures in proteins. It can be related to a general feature of the solid state assembly of cyclic peptoids: CH_2 groups in peptoids replace NH groups in peptides to form backbone to backbone hydrogen bonds (Tedesco *et al.*, 2014; Meli *et al.*, 2016; Tedesco *et al.*, 2016).

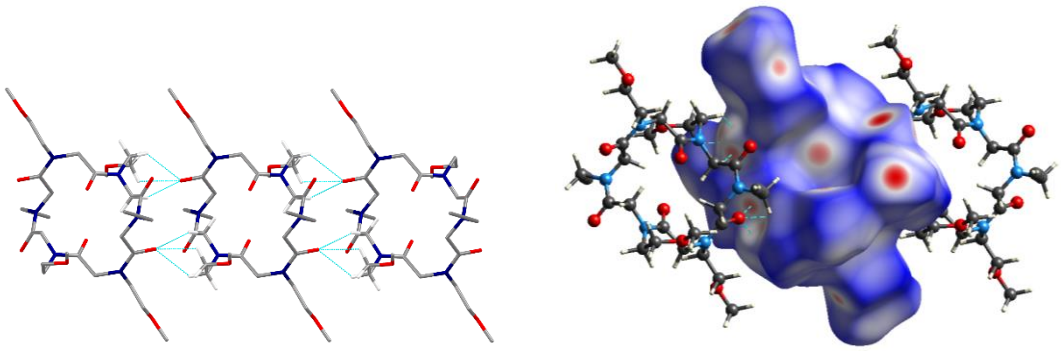

Figure 15 Side by side interactions in form **II** along the *a* axis (motif 1). CO···HC hydrogen bonds are depicted as light blue dotted lines. Oxygen atoms in red, carbon atoms in grey, nitrogen atoms in blue and hydrogen atoms in white.

Motif 2 is made by molecules related by the crystallographic screw axis. They interact by means of backbone to side chain hydrogen bonds involving the *cis* carbonyl oxygen atom O1, that connects both the propargyl hydrogen atom H5 (CO···HC = 2.08 Å; O···H-C = 166°) and the methylene hydrogen atom of the *cis* methoxyethyl side chain (H14B) (O···HC = 2.39 Å; O···H-C = 153°) belonging to two different molecules aligned along the *b* axis (Figures 9 and 16).
Thus, side by side backbone to backbone interactions among cyclic peptoids form one dimensional ribbons along the *a* axis (motif 1 in Table 5) interlaced at 1/2 *b* by backbone to side chain interactions (motif 2 in Table 5 and Figure 16). In Figure 9 shaded and white areas highlight molecular ribbons shifted by 1/2 along the *b* axis.
The packing coefficients for crystal forms **I** and **II** are 0.761 and 0.721, respectively.

Hirshfeld fingerprint plots (Spackman & McKinnon, 2002) for crystal forms **I** and **II**, respectively, are reported in Figure 17. In the case of crystal form **II** the fingerprint plot extends beyond 2.4 Å. Thus, the shape of the fingerprint plots shows a more efficient packing in case of form **I** with respect to form **II**.

Noteworthy the fingerprint plot for type A molecules is more compact with respect to type B molecules and features a sharp right spike at the bottom due to the interaction of type A molecules with water molecules (indicated by a circle in Figure 17 a). Thus, water molecules allow for an efficient columnar packing of cyclic peptoid molecules, in particular type A molecules.

This is another general feature of the cyclopeptoid solid state assembly: guest molecules from the crystallization solvents or ambient humidity contribute to favour the columnar arrangement of cyclic peptoid molecules.

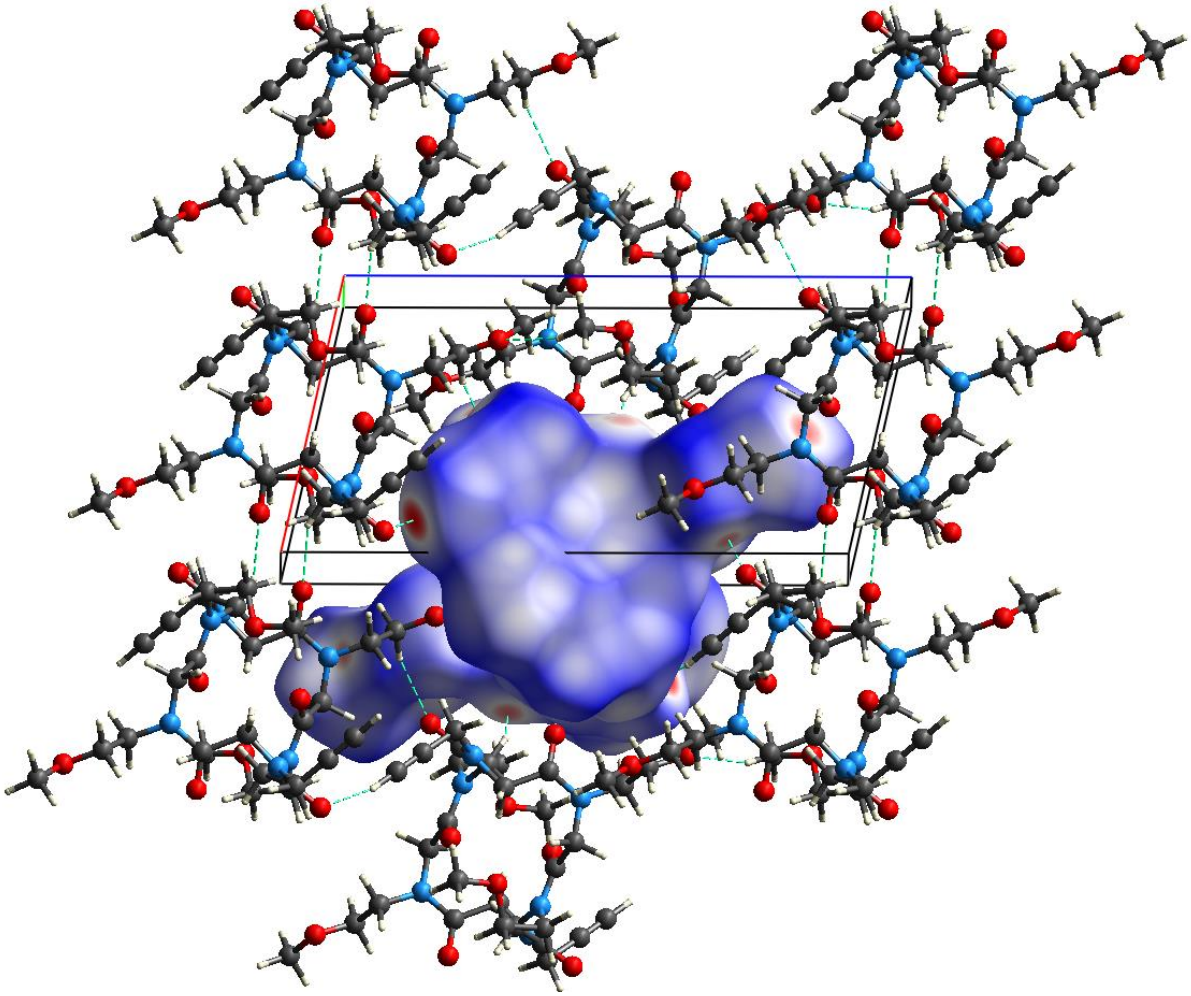

Figure 16 Intermolecular interactions between molecules related by the crystallographic screw axis in form **II** (motif 2). CO···HC hydrogen bonds are depicted as light blue dotted lines. Oxygen atoms in red, carbon atoms in grey, nitrogen atoms in blue and hydrogen atoms in white.

In absence of water molecules, as it occurs in crystal form **II**, side by side interactions among cyclic peptoids take place forming ribbons interlaced at different height by backbone to side chain interactions. This gives rise though to a less efficient packing.

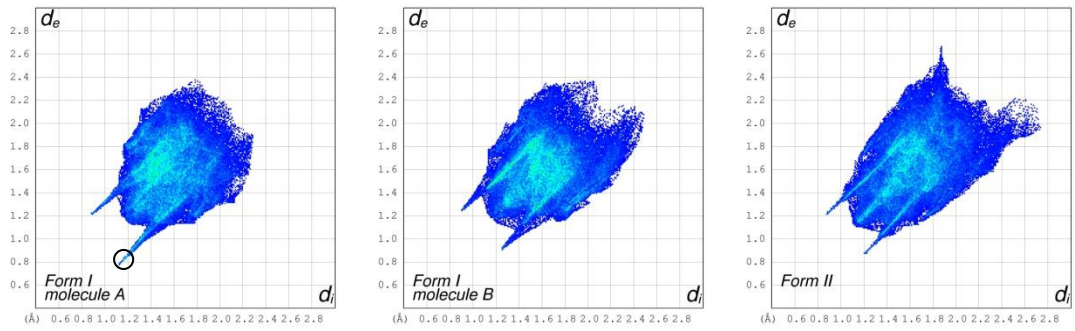

Figure 17 Hirshfeld fingerprint plots for crystal forms **I** and **II**.

Table 5 List of intermolecular distances (Å), angles (°) and interaction energies (kJ/mol) in crystal forms **I** and **II**.

Motif	**D-H···A**	**D···A** dist.	**H···A** dist.	**<D-H···A** angle	**Symm. Op.**	**Centre of mass distance**	E_{coul}	E_{pol}	E_{disp}	E_{rep}	E_{tot}
Form I											
1 A-A	C5A-H5A···O2A	3.073	2.09	150	-1+*x*, *y*, *z*	8.363	-59.9	-24.6	-88.3	85.9	-86.9
2 A-A	C8A-H8A2 ···O3A	3.257	2.27	151	*x*, -1+*y*, *z*	9.394	-35.0	-16.0	-54.6	51.1	-54.6
3 A-A	C3A-H3A1···O1A	3.360	2.58	128	-1+*x*, 1+*y*, *z*	11.854	-4.3	-5.7	-13.7	9.3	-14.4
4 B-B	C5B-H5B···O3B	3.227	2.16	170	-1+*x*, *y*, *z*	8.363	-52.8	-17.9	-69.2	62.5	-77.5
5 B-B	C8B-H8B2···O1B	3.612	2.57	162	*x*, -1+*y*, *z*	9.394	-34.0	-13.4	-62.0	38.8	-70.6
6 A-B	C10A-H10C···O3B	3.352	2.65	122	*x*, *y*, *z*	11.694	-13.4	-6.4	-47.7	26.9	-40.6
7 A-B	C11B-H11C···O5A	3.514	2.60	142	*x*, *y*, 1+*z*	11.512	-13.2	-6.1	-49.9	32.1	-37.1
8 A-B	C3B-H3B1···C14A	3.865	2.90	149	*x*, -1+*y*, +1+*z*	13.733	-4.1	-2.3	-13.2	7.2	-12.4
9 A-B	C9B-H9B1···C15A	3.693	2.77	143	*x*, 1+y, *z*	13.234	0.6	-1.2	-8.9	5.4	-4.1
10 A-W	O1W-H2W···O1A	2.860	1.88	168	-1+*x*, *y*, *z*	6.085	-38.4	-15.4	-14.6	38.7	-29.8
11 A-W	O1W-H1W···O3A	2.927	1.95	165	-1+*x*, -1+*y*, *z*	6.169	-33.8	-11.8	-12.2	27.6	-30.2
12 B-W	C3B-H3B2···O1W	3.227	2.51	123	*x*, -1+*y*, *z*	9.960	-5.8	-1.8	-3.3	4.4	-6.6
13 B-W	C15B-H15E···O1W	3.620	2.55	170	*x*, y, *z*	8.123	-2.8	-2.6	-5.2	6.5	-4.2
Form II											
1	C1-H1B···O3	3.329	2.34	152	-1+*x*, *y*, *z*	9.037	-33.4	-20.9	-60.1	57.5	-56.9
2	C5- H5···O1 C14-H14B···O1	3.141 3.393	2.08 2.39	166 153	1/2-*x*,-1/2+*y*, -1/2-*z*	10.582	-43.1	-15.7	-38.2	45.5	-51.6
3	C10-H10C···C12	3.742	2.86	139	*x*, -1+*y*, *z*	10.622	-7.4	-7.4	-57.0	34.5	-37.3
4	C10-H10A··· O5	3.439	2.39	162	1/2-*x*, 1/2+*y*, 1/2-z	12.152	-20.6	-8.4	-36.3	34.7	-30.6

3.5. Thermal analyses

As shown in Figures 18 and 19, DSC and thermogravimetric analysis on crystals of form **I** showed a rather complex thermal behaviour. Water molecules are released around 100 °C, the observed percentage weight loss (2.3%) is consistent with the value calculated by considering that in the X-ray crystal structure there is one water molecule per cyclopeptoid molecule (2.7%).

An endothermic transformation occurs at 163 °C followed by an exothermic transformation at 165 °C, finally melting occurs at 198 °C followed by decomposition starting after 230 °C.

DSC analysis on crystals of form **II** showed a small endothermic peak at 180 °C suddenly followed by a small exothermic peak at 183 °C, then melting occurs at 199 °C (Figure 20).

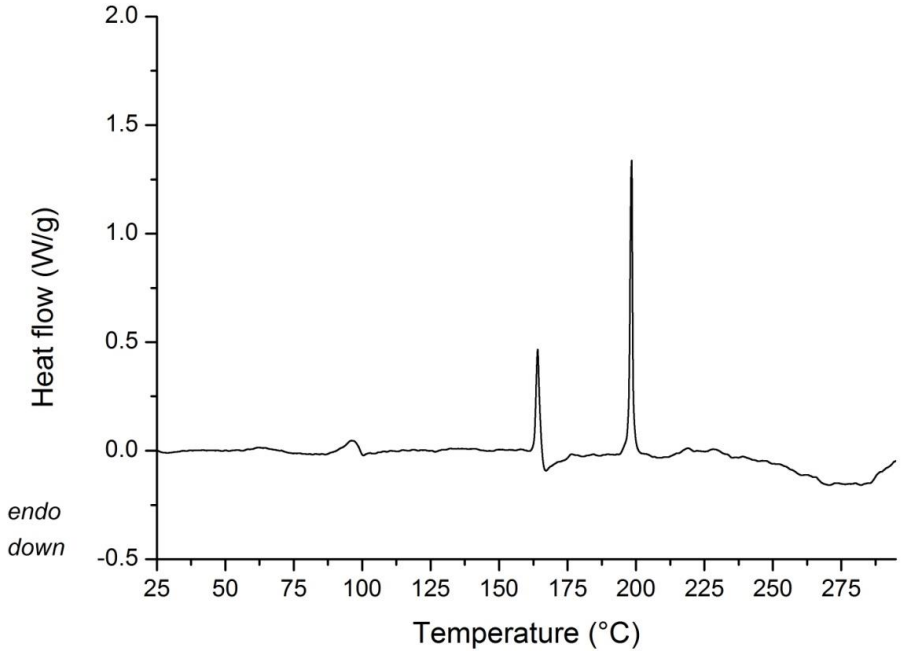

Figure 18 DSC analysis on crystals of form **I**. Water molecules are released around 100 °C. An endothermic transformation occurs at 163 °C followed by an exothermic transformation at 165 °C. Melting occurs at 198 °C followed by decomposition starting after 230 °C.

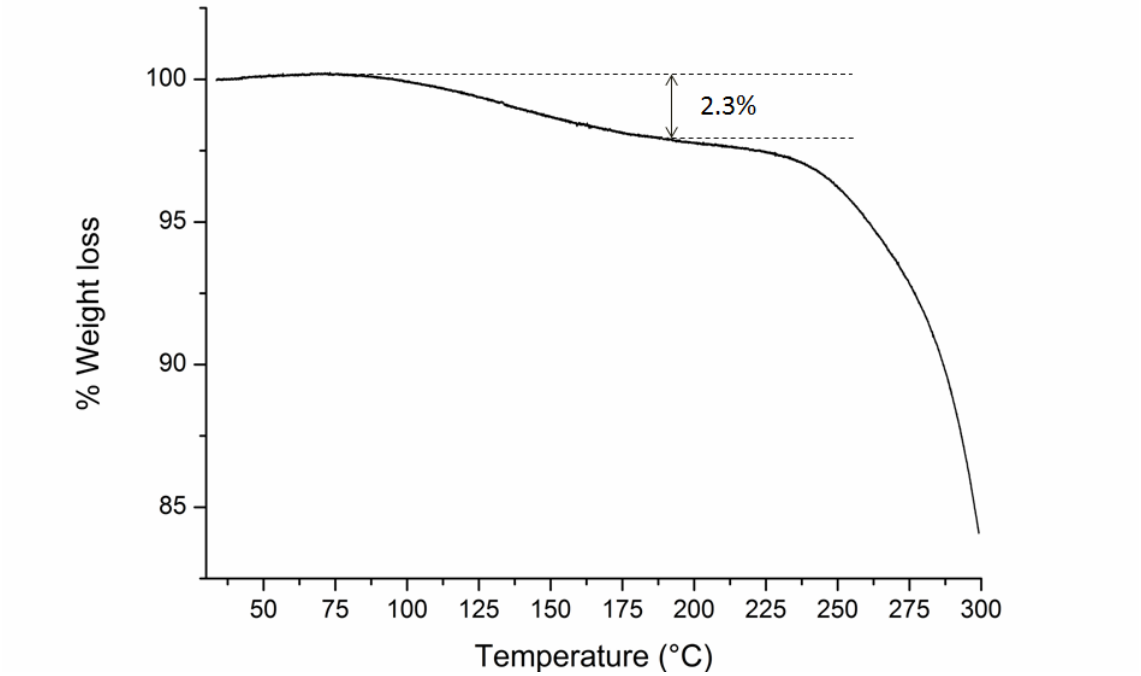

Figure 19 TGA analysis on crystals of form I.

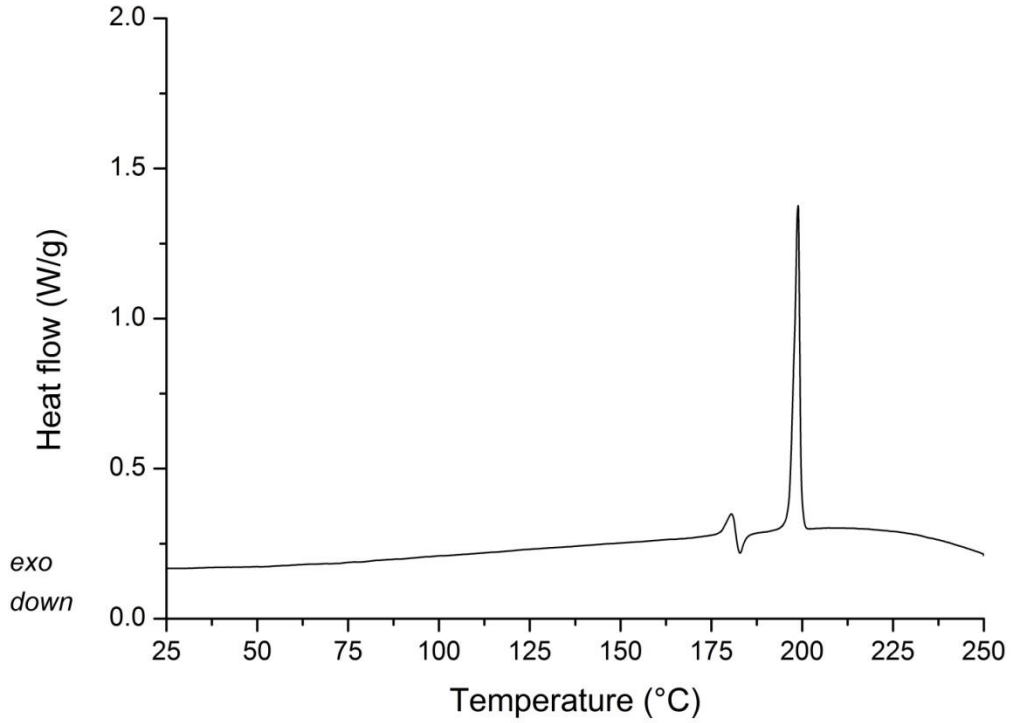

Figure 20 DSC analysis on crystals of form **II**. A small endothermic peak at 180 °C is suddenly followed by a small exothermic peak at 183 °C, thenelting occurs at 199 °C.

3.6. Quantitative phase analysis

Quantitative phase analysis was performed by Rietveld refinement and showed that BATCH1 and BATCH2 contain both crystal forms **I** and **II** in significantly different amounts (Figures 21, 22 and Table 6). BATCH1 contains 80.2 % of form **I** and BATCH2 contains 69.9 % of form **II**.

The different composition of the two batches explains the different solubility observed, resulting BATCH2 less soluble in chloroform and isopropanol than BATCH1.

Moreover, the use of EG as dehydrating agent allows the formation of single crystals of the anhydrous crystal form (form **II**) although starting from the more hydrated BATCH1.

Table 6 Rietveld refinement results for BATCH1 and BATCH2.

Sample	R_p fitted	R_{wp} fitted	R_F^2 Form I	R_F^2 Form II	% Form I	% Form II
BATCH1	0.085	0.110	0.027	0.037	80.2	19.8
BATCH2	0.054	0.070	0.024	0.041	30.1	69.9

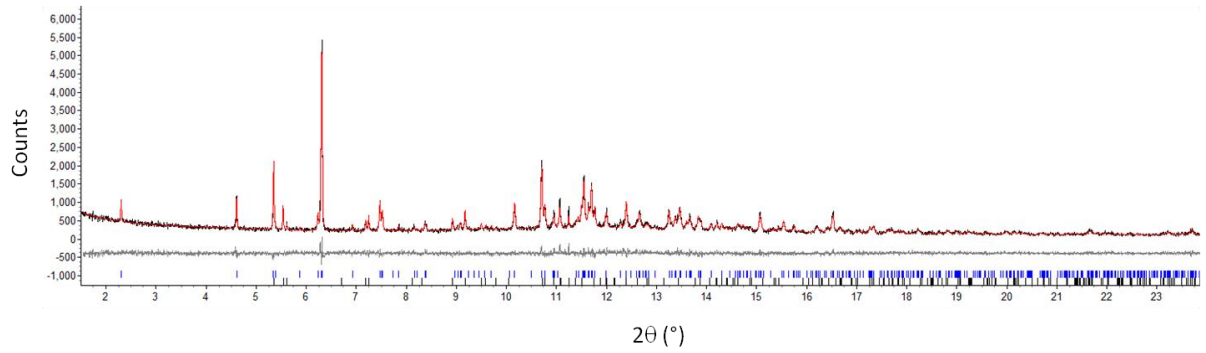

Figure 21 Rietveld refinement results for BATCH1 at 100 K. Observed (black line) and calculated (red line) X-ray powder diffraction profiles as well as difference profile (grey line) are shown. Calculated reflections for crystal form **I** and crystal form **II** are indicated, respectively, with blue and black bars.

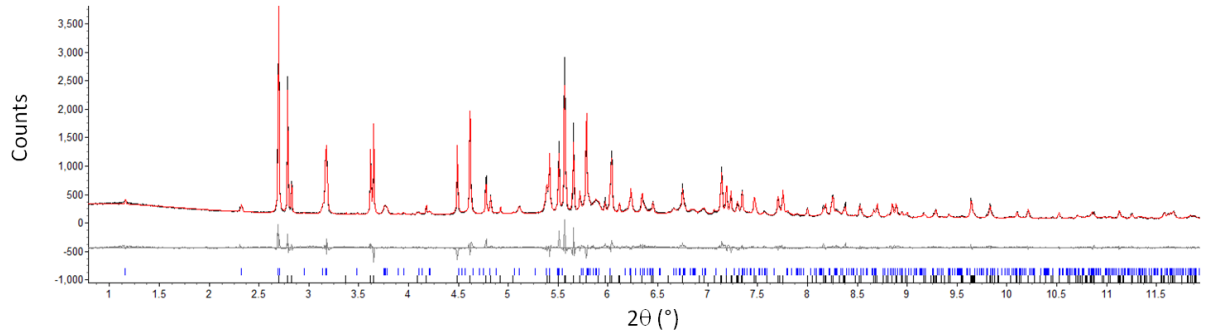

Figure 22 Rietveld refinement results for BATCH2 at 100 K. Observed (black line) and calculated (red line) X-ray powder diffraction profiles as well as difference profile (grey line) are shown. Calculated reflections for crystal form **I** and crystal form **II** are indicated, respectively, with blue and black bars.

4. Conclusions

We described the synthesis and the structural characterization of a cyclic hexapeptoid with four methoxyethyl and two propargyl side chains.

We obtained a hydrate crystal form (form **I**) and an anhydrous crystal form (form **II**) from the purified product. The relative amounts of form **I** and form **II**, as determined by XRPD quantitative phase analysis, depend on the purification procedures.

In the crystal form **I** peptoid molecules assemble in a columnar arrangement as the propargyl side chains act as pillars between the macrocycles planes by means of C≡CH···OC hydrogen bonds.

In the anhydrous crystal form **II** cyclopeptoid molecules form ribbons by means of CH_2···OC backbone to backbone interactions, thus mimicking beta-sheet secondary structures in proteins.

In both crystal forms side chains act as joints among the columns or the ribbons and contribute to the stability of the whole solid state assembly.

The more efficient packing of the hydrate crystal form **I** with respect to the anhydrous crystal form **II** highlights the role of the water molecules, that bridge columns of cyclic peptoid molecules and stabilize a columnar arrangement.

Acknowledgements The research leading to these results has received funding from the People Programme (Marie Curie Actions) of the European Union's Seventh Framework Programme FP7/2007-2013/ under REA grant agreement n°PIRSES-GA-2012-319011. ESRF is acknowledged for beam time at beam lines ID11 (proposal # CH-3861) and ID22 (proposal # CH-4166). Financial support also from the University of Salerno (FARB).

References

Allen, F. H., Kennard, O., Watson, D. G., Brammer, L., Orpen, A. G.& Taylor, R. (1995). *International Tables for Crystallography*, ed. A. J. C. Wilson, pp. 685–706, Kluwer Academic, Dordrecht.

Ambrosi, G., Formica, M., Fusi, V., Giorgi, L., Macedi, E., Micheloni M. & Pontellini, R. (2009a). *Inorg. Chim. Acta* **362**, 2667-2677.

Ambrosi, G., Battelli, C., Formica, M., Fusi, V., Giorgi, L., Macedi, E., Micheloni, M., Pontellini R. & Prodi, L. (2009b). *New J. Chem.* **33**, 171–180.

Ambrosi, G., Formica, M., Fusi, V., Giorgi, L., Macedi, E., Micheloni, M., Piersanti G. & Pontellini, R. (2010). *Org. Biomol. Chem.* **8**, 1471–1478.

Böhmer, V. (1995). *Angew. Chem. Int. Ed. Engl.* **34**, 713–745.

Bruker (2012). SMART, SAINT, SADABS. Bruker AXS Inc., Madison, Wisconsin, USA. Bruker AXS Inc., Madison, Wisconsin, USA.

Burla, M. C., Caliandro, R., Carrozzini, B., Cascarano, G. L., Cuocci, C., Giacovazzo, C., Mallamo, M., Mazzone, A. & Polidori, G. (2015). *J. Appl. Cryst.* **48**, 306–309.

Butterfoss, G. L., Renfrew, P. D., Kuhlman, B., Kirshenbaum, K. & Bonneau, R. (2009). *J. Am. Chem. Soc.***131**,16798–807.

Coelho, A. A. (2007). TOPAS-Academic V4.1.

Comegna, D., Benincasa, M., Gennaro, R., Izzo, I. & De Riccardis, F. (2010). *Bioorg. Med. Chem.* **18**, 2010-8.

Crawford, J. L., Lipscomb, W. N. & Schellman, C. G. (1973). *Proc. Nat. Acad. Sci. USA* **70**, 538-542.

CrystalClear (2006). Crystal Structure Analysis Package, Rigaku-Molecular Structure Corp.

Culf, A. S. & Ouellette, R. J. (2010). *Molecules* **15**, 5282–5335.

De Cola, C., Licen, S., Comegna, D., Cafaro, E., Bifulco, G., Izzo, I., Tecilla, P. & De Riccardis, F. (2009). *Org. Biomol. Chem.* **7**, 2851-2854.

Della Sala, G., Nardone, B., De Riccardis F. & Izzo, I. (2013). *Org. & Biomol. Chem.*, **11**, 726–731.

Dietrich, P., Viout, P. & Lehn, J.-M. (1993). *Macrocyclic Chemistry*. VCH,Weinheim.

Dolomanov, O. V., Bourhis, L. J., Gildea, R. J., Howard, J. A. K. & Puschmann, H. (2009). *J. Appl. Cryst.* **42**, 339–341.

Gangloff, N., Ulbricht, J., Lorson, T., Schlaad, H. & Luxenhofer, R. (2016). *Chem. Rev.* **116**, 1753−1802.

Finger, L. W., Cox, D. E. & Jephcoat, A. P. (1994). *J.Appl. Cryst.* **27**, 892−900.

Fitch, A. N. (2004). *Res. Natl. Inst. Stand. Techno*l. **109**, 133−142.

Gavezzotti, A. (2002). *J. Phys. Chem. B* **106**, 4145–4154.

Gavezzotti, A. (2003). *J. Phys. Chem. B* **107**, 2344–2353.

Gavezzotti, A. (2011). *New J. Chem.* **35**, 1360–1368.

Gokel, G. W. (1992). *Crown Ethers and Cryptands (Monographs in Supramolecular Chemistry)*, ed. J. F. Stoddart, Royal Society of Chemistry, Cambridge.

Huang, M. L., Shin, S. B. Y., Benson, M. A., Torres, V. J. & Kirshenbaum, K. (2012). *ChemMedChem* **7**, 114–122.

Huang, M. L., Benson, M. A., Shin, S. B. Y., Torres, V. J. & Kirshenbaum, K. (2013). *Eur. J. Org. Chem.* 3560–3566.

Izzo, I., De Cola, C. & De Riccardis, F. (2011). *Heterocycles* **82**, 981–1006.

Izzo, I., Ianniello, G., De Cola, C., Nardone, B., Erra, L., Vaughan, G., Tedesco, C. & De Riccardis, F. (2013). *Org. Lett.* **15**, 598–601.

Lepage, M. L., Meli, A., Bodlenner, A., Tarnus, C., De Riccardis, F., Izzo, I. & Compain, P. (2014). *Beilstein J. Org. Chem.* **10**, 1406–1412.

Lepage, M. L., Schneider, J. P., Bodlenner, A., Meli, A., De Riccardis, F., Schmitt, M., Tarnus, C., Nguyen-Huynh, N.-T., Francois, Y.-N., Leize-Wagner, E., Birck, C., Cousido-Siah, A., Podjarny, A., Izzo, I. & Compain, P. (2016). *Chem. Eur. J.* **22**, 5151−5155.

Macrae, C. F., Bruno, I. J., Chisholm, J. A., Edgington, P. R., McCabe, P., Pidcock, E., Rodriguez-Monge, L., Taylor, R., van de Streek, J. & Wood, P. A. (2008). *J. Appl. Crystallogr*. **41**, 466–470.

Maulucci, N., Izzo, I., Bifulco, G., Aliberti, A., De Cola, C., Comegna, D., Gaeta, C., Napolitano, A., Pizza, C., Tedesco, C., Flot, D. & De Riccardis, F. (2008). *Chem. Commun*., 3927–3929.

McKinnon, J. J., Spackman, M. A. & Mitchell, A. S. (2004). *Acta Crystallogr., Sect. B: Struct. Sci*. **60**, 627–668.

McKinnon, J. J., Jayatilaka, D. & Spackman, M. A. (2007). *Chem. Commun*. 3814– 3816

Meli, A., Macedi, E., De Riccardis, F., Smith, V. J., Barbour, L. J., Izzo, I. & Tedesco, C. (2006). *Angew. Chem. Int. Ed. Engl.* **55**, 4679–4682.

Schettini, R., Nardone, B., De Riccardis, F., Della Sala, G. & Izzo, I (2014). *Eur. J. Org. Chem.* 7793–7797.

Schettini, R., De Riccardis, F., Della Sala, G. & Izzo, I (2016). *J. Org. Chem.* **81**, 2494−2505.

Sheldrick, G. M. (2015). *Acta Cryst*. **C71**, 3–8.

Shin, S. B. Y., Yoo, B., Todaro, L. J. & Kirshenbaum, K. (2007). *J. Am. Chem. Soc.* **129**, 3218–3225.

Shukla, R.,Mohan, T. P., Vishalakshi, B. & Chopra, D. (2014). *CrystEngComm* **16**, 1702–1713.

Solanko, K. A. & Bond, A. D. (2011). *Acta Cryst.* **B67**, 437–445

Spackman, M. A. & McKinnon, J. J. (2002). *CrystEngComm* **4**, 378–392.

Spackman, M. A. & Jayatilaka, D. (2009). *CrystEngComm* **11**, 19–32.

Spackman, M. A. (2013). *Phys. Scr.* **87,** 048103. doi:10.1088/0031-8949/87/04/048103

Sun, J. & Zuckermann, R. N. (2013). *ACS Nano* **7**, 4715–4732.

Tedesco, C., Erra, L., Izzo, I. & De Riccardis, F. (2014). *CrystEngComm* **16**, 3667−3687.

Tedesco, C., Meli, A., Macedi, E., Iuliano, V., Ricciardulli, A. G., De Riccardis, F., Vaughan G. B. M., Smith, V. J., Barbour, L. J. & Izzo, I. (2016). *CrystEngComm*, DOI: 10.1039/C6CE01800A.

Venkatachalam, C. M. (1968). *Biopolymers* **6**, 1425-1436.

Wolff, S. K., Grimwood, D. J., McKinnon, J. J., Turner, M. J., Jayatilaka, D. & Spackman, M. A. (2013). CrystalExplorer (Version 3.1), University of Western Australia, 2013.

Yoo, B., Shin, S. B. Y., Huang, M. L. & Kirshenbaum, K. (2010). *Chem. Eur. J.* **16**, 5528–5537.

Zuckermann, R. N., Kerr, J. M., Kent, S. B. H., Moos, W. H. (1992). *J. Am. Chem. Soc.* **114**, 10646–10647.

Supporting information

S1. List of abbreviations

DIC *N*,*N*′-diisopropyl carbodiimide; HFIP = 1,1,1,3,3,3-hexafluoro-2-propanol.

DIPEA *N*,*N*-diisopropylethylamine

DMSO dimethylsulfoxide

DSC Differential scanning calometry

TGA Thermogravimentric analysis

DVB divinylbenzene

EG Ethylene glycol

HATU 1-[bis(dimethylamino)methylene]-1*H*-1,2,3-triazolo[4,5-*b*]pyridinium hexafluorophosphate 3-oxide

Npa *N*-(propargyl)glycine

Nme *N*-(methoxyethyl)glycine

S2. Synthesis

S2.1. General procedures

Starting materials and reagents purchased from commercial suppliers were generally used without purification unless otherwise mentioned. HPLC analysis were performed on a JASCO LC-NET II/ADC equipped with a JASCO Model PU-2089 Plus Pump and a JASCO MD-2010 Plus UV-vis multiple wavelength detector set at 220 nm. The column used was a C_{18} reversed-phase analytical column (Waters, Bondapak, 10 μ m, 125 Å, 3.9 mm × 300 mm) run with linear gradients of ACN (0.1% TFA) into H_2O (0.1% TFA) over 30 min, at a flow rate of 1.0 mL/min for the analytical runs. ESI-MS analysis in positive ion mode was performed using a Finnigan LCQ Deca ion trap mass spectrometer (ThermoFinnigan, San Josè, CA, USA) and the mass spectra were acquired and processed using the Xcalibur software provided by Thermo Finnigan. Samples were dissolved in 1:1 CH_3OH/H_2O, 0.1 % formic acid, and infused in the ESI source by using a syringe pump; the flow rate was 5 μl/min. The capillary voltage was set at 4.0 V, the spray voltage at 5 kV, and the tube lens offset at -40 V. The capillary temperature was 220 °C. Data were acquired in MS^1 and MS^n scanning modes. Zoom scan was used in these experiments. High-resolution ESI-MS spectra were recorded on a Q-Star Applied Biosystem mass spectrometer. NMR spectra were recorded on a Bruker DRX 400 (^{1}H at 400.00 MHz, ^{13}C at 100.00 MHz). Chemical shifts (δ) are reported in ppm relative to the

residual solvent peak ($CDCl_3$, δ = 7.26; $^{13}CDCl_3$, δ = 77.0) and the multiplicity of each signal is designated by the following abbreviations: s, singlet; d, doublet; t, triplet; m, multiplet; bs, broad singlet. Coupling constants (J) are quoted in Hertz.

S2.2. NMR Spectra

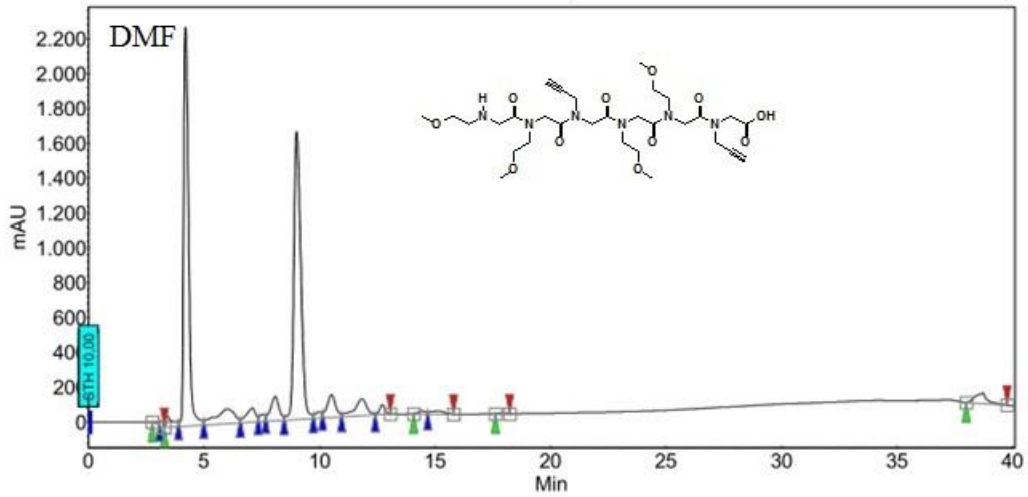

(a)

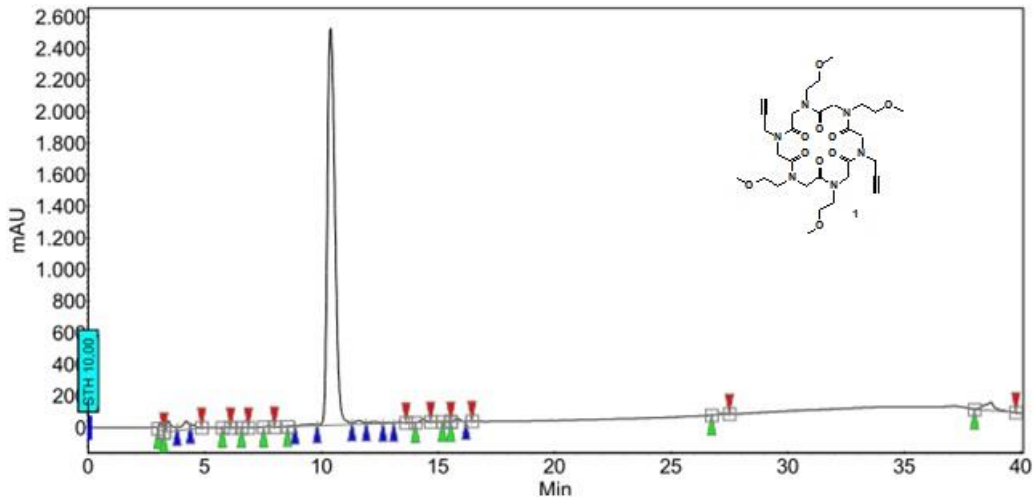

(b)

Figure S1 HPLC chromatograms: (a) linear precursor of compound **1**; (b) compound **1**. Conditions: 5 → 100% A in 30 min (A, 0.1% TFA in acetonitrile, B, 0.1% TFA in water); flow: 1 mL min^{-1}, 220 nm.

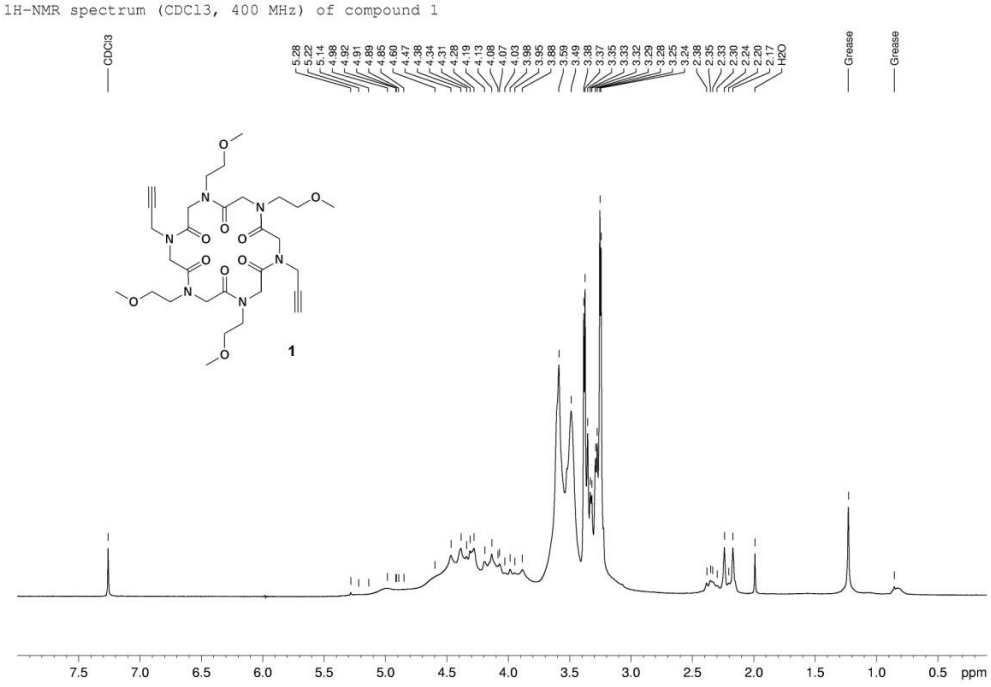

Figure S2 ^{1}H-NMR (400 MHz, $CDCl_3$) spectrum of compound **1**

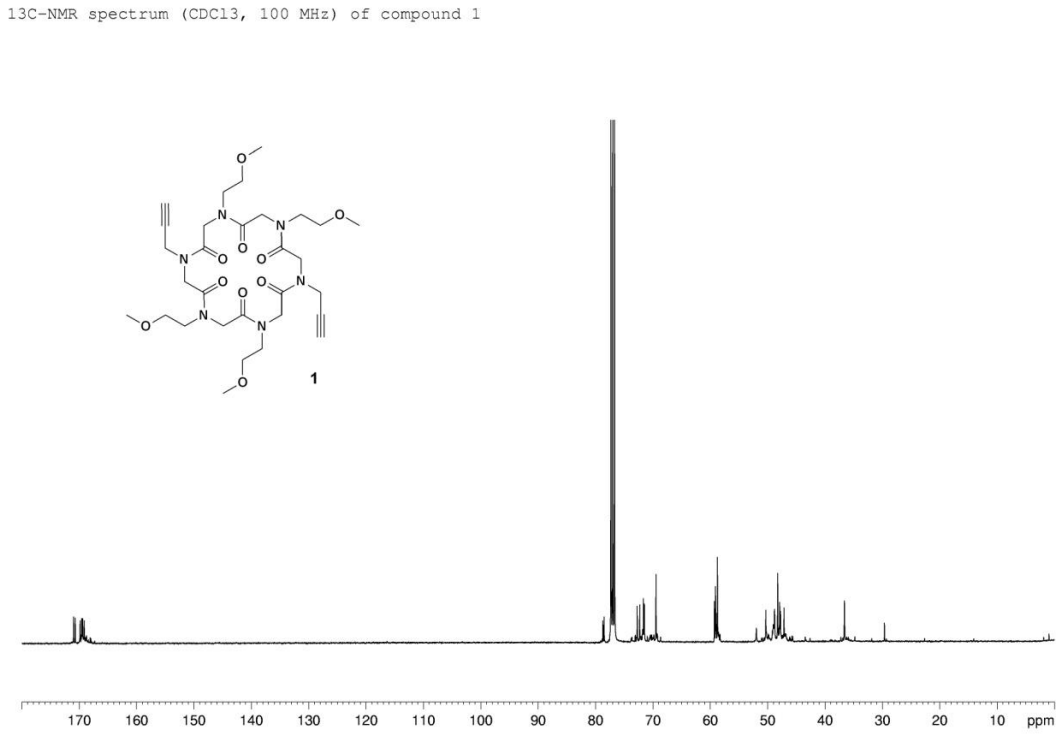

Figure S3 ^{13}C-NMR (100 MHz, CDCl3) spectrum of compound **1**

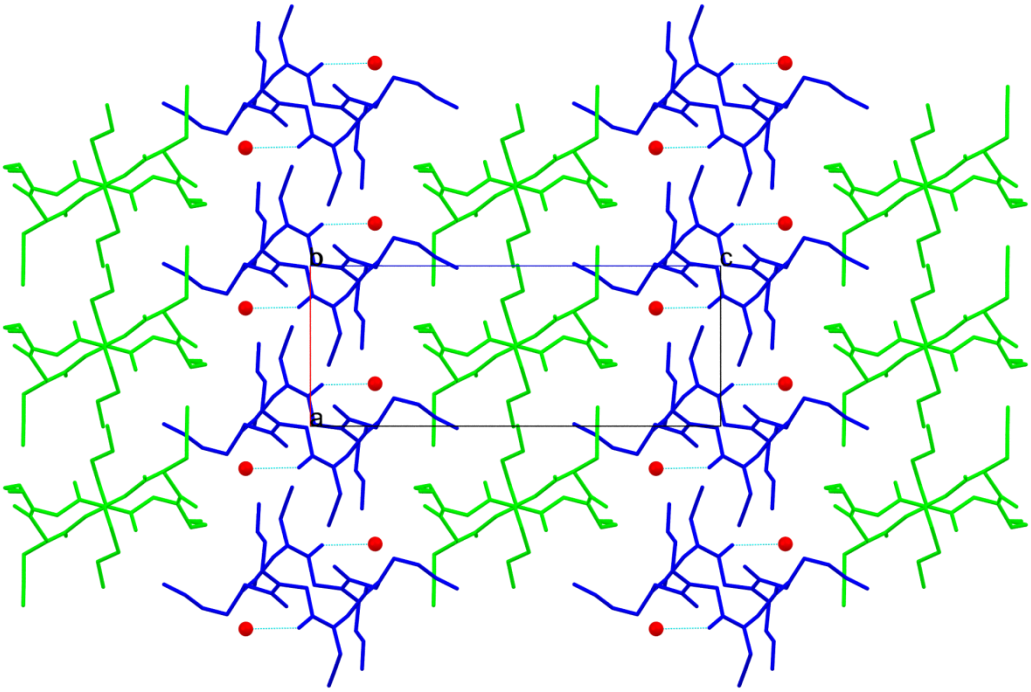

Figure S4 Crystal packing of form **I** as viewed along the *b* axis. Hydrogen atoms have been omitted for clarity. Type A molecules are shown in blue and type B molecules in green. Water molecules are depicted in red in ball and stick style. Hydrogen bonds are depicted as light blue dotted lines.

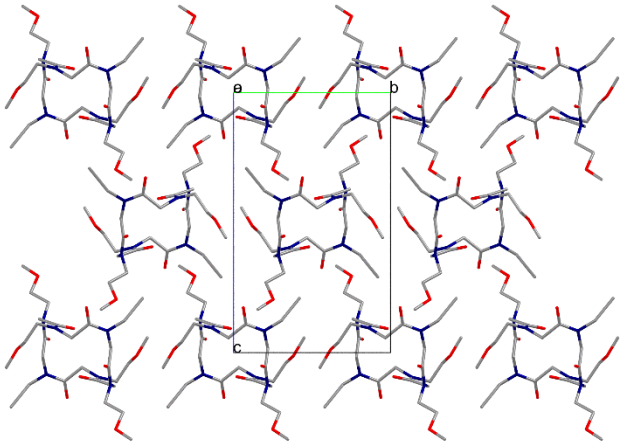

Figure S5 Crystal packing of form **II** as viewed along the *a* axis. Hydrogen atoms have been omitted for clarity. Oxygen atoms in red, carbon in grey, nitrogen in blue.

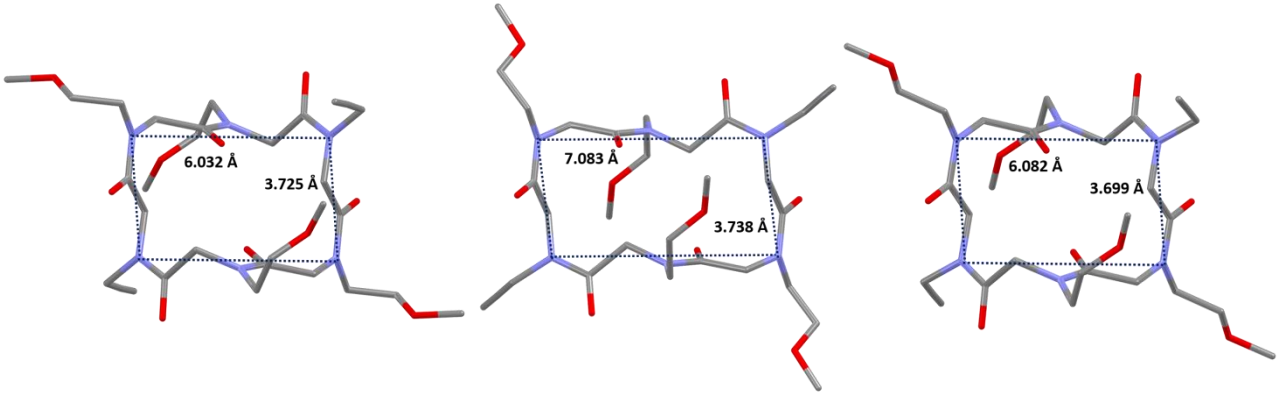

a b c

Figure S6 Rectangular shape of the macrocycles in: a) crystal form **I**, type A; crystal form **I**, type B; crystal form **II**. Hydrogen atoms have been omitted for clarity. Oxygen atoms in red, carbon grey, nitrogen blue.

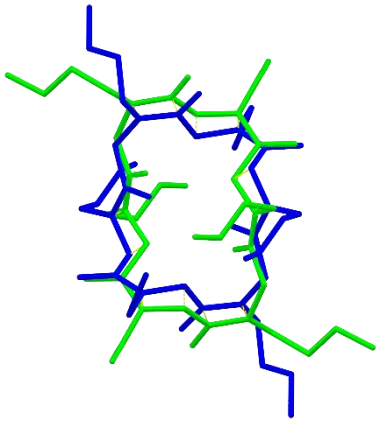

Figure S7 Backbone superimposition of the type A (blue) and type B molecules (green) in form **I**, rmsd 0.647 Å.

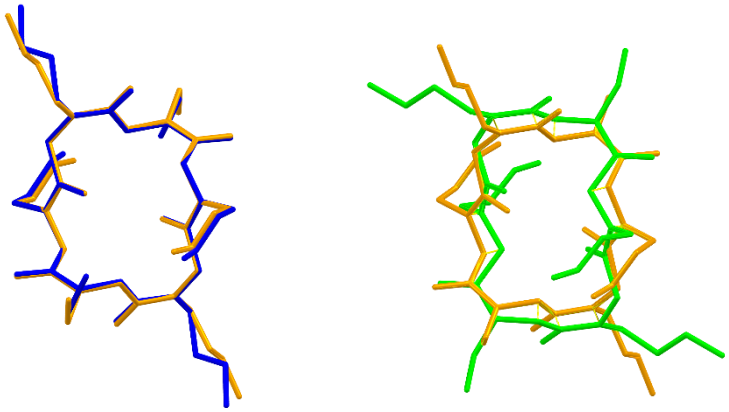

(a) (b)

Figure S8 (a) Backbone superimposition of type A cyclopeptoid molecule in crystal form **I** (blue) and the cyclopeptoid molecule in form **II** (orange), rmsd 0.0435 Å; (b) backbone superimposition of type B molecule in form **I** (green) and form **II** (orange), rmsd 0.622 Å.

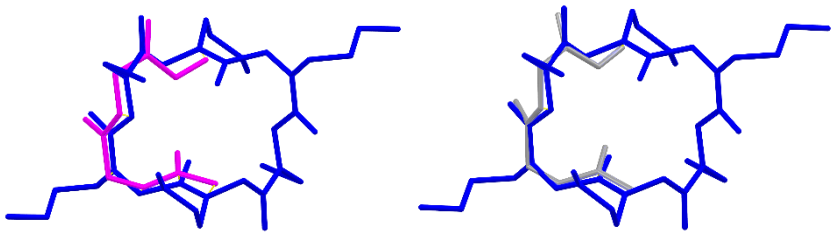

Figure S9 Superposition of the backbone atoms of type A cyclopeptoid molecules in crystal form **I** with idealized type I (magenta) and type III (silver) *beta*-turn peptide.

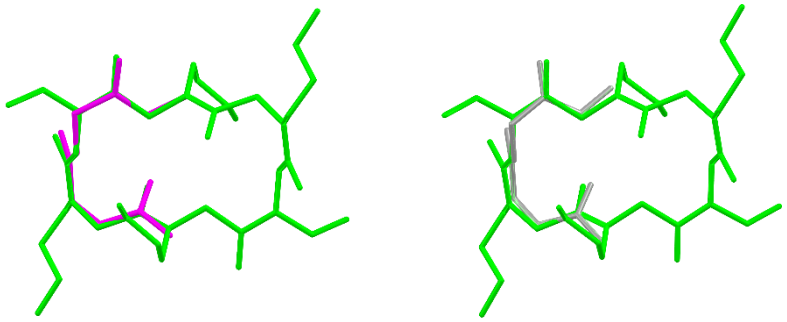

Figure S10 Superposition of the backbone atoms of type B cyclopeptoid molecules in crystal form **I** with idealized type I (magenta) and type III (silver) *beta*-turn peptide.

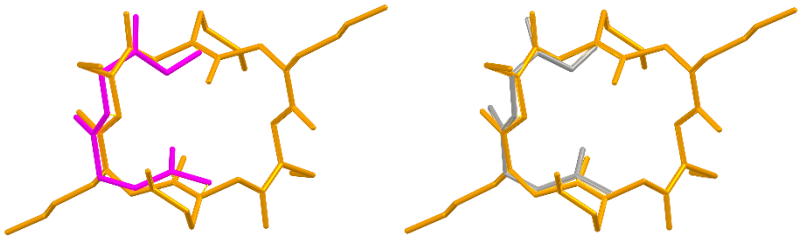

Figure S11 Superposition of the backbone atoms of the cyclopeptoid molecule in crystal form **II** with idealized type I (magenta) and type III (silver) *beta*-turn peptide.

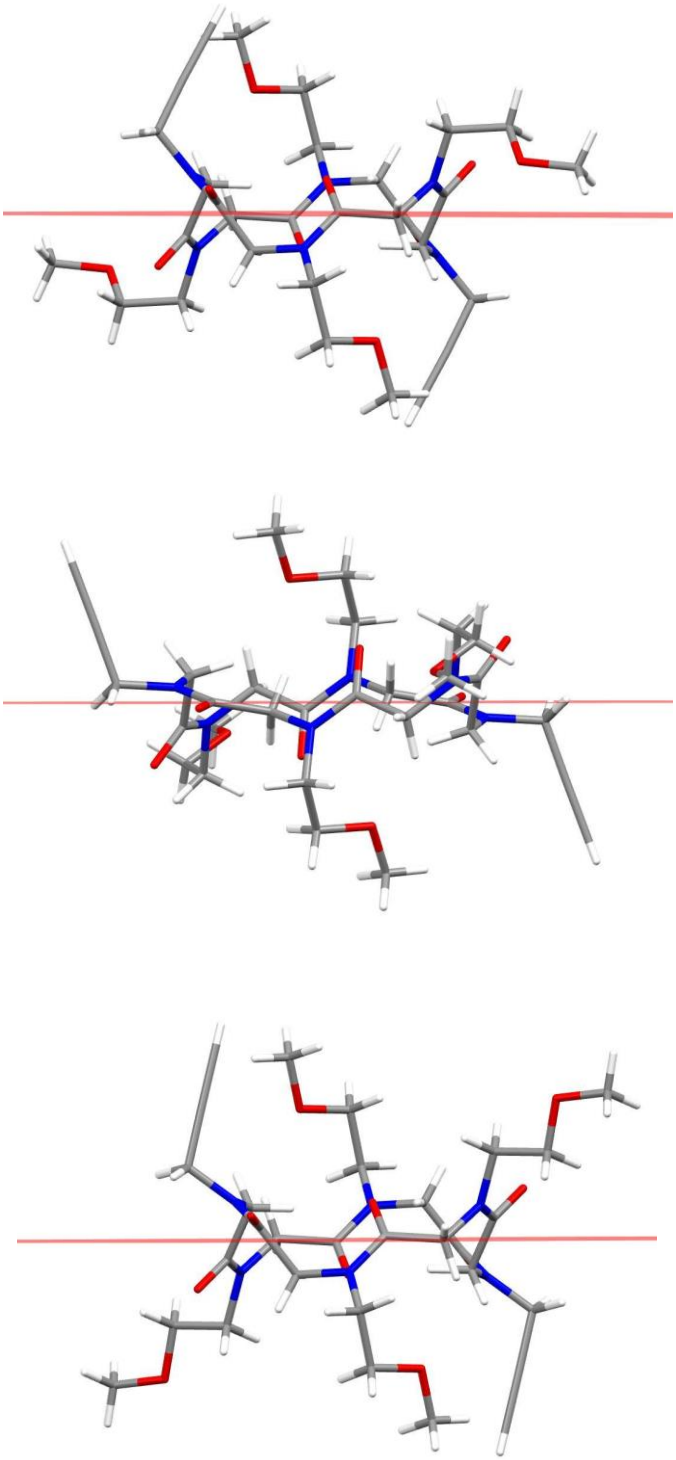

Figure S12 Side chains orientation with respect to the macrocycle plane in crystal forms **I**, type A (top) and type B molecule (middle), and **II** (bottom): two *trans* methoxyethyl and two *cis* propargyl side chains point vertically, two *cis* propargyl side chains extend horizontally.

S3. Hirshfeld surface analysis

The Hirshfeld surface arises from the partitioning of the electron density of a crystal into molecular fragments (McKinnon *et al.*, 2004; Spackman & Jayatilaka, 2009). It provides maximum proximity of neighbouring molecular volumes without volumes overlapping (Spackman, 2013).

d_i is the distance from the surface to the nearest atom interior to the surface. d_e is the distance from the surface to the nearest atom exterior to the surface. d_{norm} is a normalized distance, which takes into account the relative atom sizes (McKinnon *et al.*, 2007):

$$d_{\mathrm{norm}} = \frac{d_i - r_i^{\mathrm{vdW}}}{r_i^{\mathrm{vdW}}} + \frac{d_e - r_e^{\mathrm{vdW}}}{r_e^{\mathrm{vdW}}}$$

where r^{vdW} is the van der Waals (vdW) radius of the appropriate atom internal or external to the surface.

Relative contributions to the Hirshfeld surface area of particular types of intermolecular contacts are determined by summing the area corresponding to close contacts between specific types of atoms. The fingerprint plots summarize quantitatively the nature and type of intermolecular interactions. *x* and *y* axes report respectively the d_i and d_e distances (Spackman & McKinnon, 2002).